Rowan University

Rowan Digital Works

Theses and Dissertations

2-1-2021

Discrete element modeling of hydrogel extrusion

Rohit Boddu
Rowan University

DISCRETE ELEMENT MODELING OF HYDROGEL EXTRUSION

By
Rohit Boddu

A Thesis

Submitted to the
Department of Mechanical Engineering
College of Engineering
In partial fulfillment of the requirement
For the degree of
Master of Science in Mechanical Engineering
at
Rowan University
January 4, 2021

Committee Chair: Amir K. Miri, Ph.D.

Dedications

I would like to dedicate this work to my parents, my advisors Amir K. Miri, Ph.D. and Cheng Zhu, Ph.D., my friends, and all the people who have supported me in my academic career.

Abstract

Rohit Boddu
DISCRETE ELEMENT MODELING OF HYDROGEL EXTRUSION
2019-2020
Amir K. Miri, Ph.D.
Master of Science in Mechanical Engineering

Hydrogels are widely used in extrusion bioprinting as bioinks. Understanding how the hydrogel microstructure affects the bioprinting process aids researchers in predicting the behavior of biological components. Current experimental tools are unable to measure internal forces and microstructure variations during the bioprinting process. In this work, discrete element modeling was used to study the internal interactions and the elastic deformation of the molecular chains within hydrogel networks during the extrusion process. Two-dimensional models of hydrogel extrusions were created in Particle Flow Code (PFC; Itasca Co., Minneapolis, MN). For our model's calibration, hydrogel compression testing was used in which a cluster of particles is pushed in the vertical direction with a confined load similar to the uniaxial compression test. The parameter sensitivity study was performed using a set of parameters, e.g., coefficient of friction, restitution coefficient, and stiffness. Force distribution among the particles during the extrusion process was then predicted using the results of the study. Using this model, we analyzed the distribution of internal forces.

Table of Contents

Table of Contents (Continued)

List of Figures

List of Figures (Continued)

List of Tables

Chapter 1

Introduction

1.1. Background

Additive manufacturing (AM) has transformed the field of engineering [1] in design and manufacturing applications. The most commonly used situations are environmental control systems (ECS), custom aircraft interior components, and rocket engine components. AM is the process that uses computer control to extrude material together layer-by-layer and therefore creating a three-dimensional (3D) object. Charles Hull printed the 3D model in 1983, plotting a new field of manufacturing processes known today as AM [2]. AM techniques were introduced in 1986 with the first stereolithography apparatus (SLA) by the American company 3D-systems. Since then, academic and industrial research has continuously worked to extend AM processes [3], appropriate materials [4], and the range of applications [5]. The stereolithographic printing apparatus was able to fabricate complicated parts, layer by layer, in a fraction of 1992 and became the first entry into rapid prototyping [6]. This 3D printing technology creates physical 3D objects by converting digital files created using Computer-Aided Design (CAD), Computer-Aided Manufacturing (CAM) or a 3D scanner. A great contribution from Charles Hull was introducing the STL file format, digital layer slicing and infill strategies that are still being used in many AM processes today. There are many different 3D printing technologies that are used in the present day, but the research presented here mainly focuses on the material extrusion technique.

Studies on developing new consumables and 3D printing methods continue to progress. The search for biological applications of 3D printing started in 1996, when the founder of Organovo studied cell behavior and noted that they could be fused into entirely different spatial structures. Biomaterials in regenerative medicine were also starting to be used. The space scaffold was first designed at Wake Forest University in 2000 and was used to make the first synthetic organ in the world. In 2003, a scientist at El Paso University introduced his design system, which is considered the first ancestor of current bioprinters.
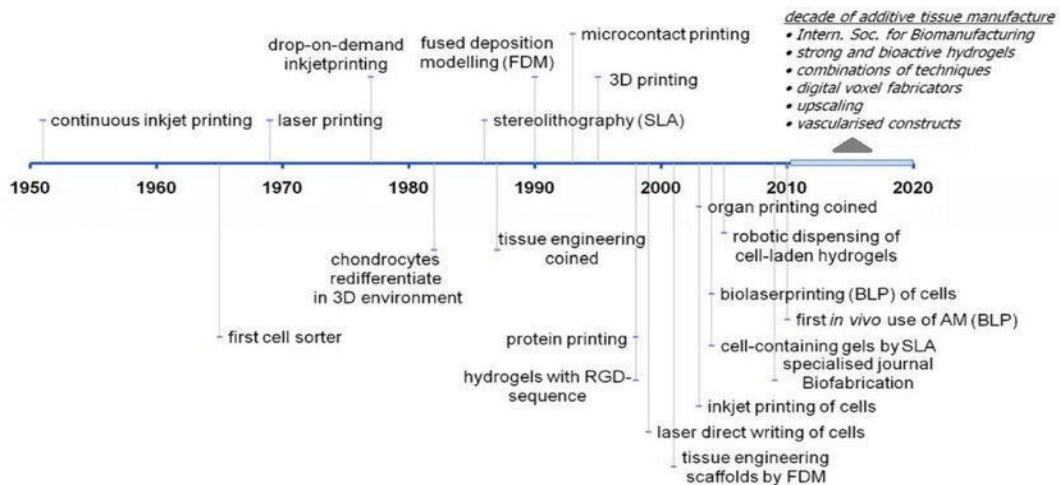
Figure 1. History of Bioprinting [7]

Dr. Forgacs made his first bioprinter appearance in 1996, resulting in a great revolution to the scientific community. It was the first instrument to permit 3D direct biodegradation without the need to create a ground, i.e., using live cells. This technology has proven to be fascinating as one of Organovo's first commercial bioprinters – NovoGen

MMX – was developed in 2009. Bioengineers then used the method to produce the first biodegraded blood vessel without using cell scaffolding several months later. The years following this marked an intense period in which research was performed to create structures such as baptismal tissue (2012), liver (2012), blood-borne network tissue (2014), and cardiovascular valve (2016).

In this era, Organovo has effectively enhanced its leading role in bioprint technology – a platform for the production and study of new medicines has been developed using biodegradable 3D tissue patterns (including cancer). For several years, the company has cooperated with L'Oréal to create artificial leather that avoids animal cosmetic research. The Swede company Cellink has launched their bioprinting system in 2015, INKREDIBLE. Another influential idea, by CELLINK, was to use other methods than the pneumatic extrusion of gel materials to design the next iterations of bioprimsers. Though there still needs to be a lot of research, the current 3D printed organs show that further innovation and discoveries are possible.

1.2. Extrusion Bioprinting

Recent bioprinting techniques have difficulties constructing relevant structures based on the appropriate resolutions defined by the detailed architecture in biological tissues. An optimal ECM-like microenvironment should include several properties, such as pore size within a range of multiple cell sizes to provide cell motility, pore interconnection to enable the diffusion of nutrients and metabolites [8], and proper surface chemistry.

Feature size is defined as the smallest size on which the tissue can be constructed while maintaining its primary function. This parameter illustrates the tissue's complex nature and specifies the degree of precision necessary for its manufacture. The sizes of the features in the structures of some tissue types are limited to submillimeter scales. For instance, a multi-layered skin consists of three single submillimeter thick layers, stacked in collaboration with several cell/ECM shapes across each layer [9]. The epidermis has a thickness of approximately 100 μm and is filled with keratinocytes tightly intertwined with a barrier. The dermis is the thickest layer and contains fibroblasts, macrophages, and adipocytes. The hypodermis layer is primarily used for fat storage and includes loose connective tissues. In this context, numerous cell-laden bioinks made of collagen, fibroblasts, and keratinocytes have been used, contributing to the formation of the basement membrane after in vitro culture [10]. The thickness of the different layers of the skin has a range of up to 100 μm. This range is enough to allow a one-to-one projection of the host tissue.

The feature size decreases in other target tissues, such as the skeletal muscle. The muscle cells, known as myocytes, are elongated cells containing myofibrils. Myofibril consists of long chains of sarcomeres situated inside a multinucleated syncytium cytoplasm and forms the skeleton muscle's structural block. [11]. The aligned assembly of myofibrils provides spatially dispersed active forces to achieve muscle functionality [12]. A few attempts have been made to generate larger muscle tissues with aligned muscle cells on thin sheets of the collagen matrix, such as those stated by Yan *et al*. [13], which implied that the micro-architecture of muscle bundles and cell alignments required a bioprinting

resolution of < 50 μm. Acellular bioinks that mimic muscle composition are suggested to develop ECM-like microenvironments that guide the activity of seeded muscle cells [14].

The bioprinting resolution is also significant in cardiac muscles due to the high sensitivity of cardiac functionality to cell alignment. The myocardium comprises cardiomyocytes and other cell types that are structured in a well-ordered arrangement, which also provides an electrical connection between the cardiac and non-cardiac cells [15]. The in vivo framework of the cardiac muscle has a reticular basket-like structure. And cardiomyocytes are rectangular and are embedded into fibers with a diameter of 100 μm [15]. To obtain functional cardiac models, cardiomyocytes should be coupled with anisotropic arrangements for electrophysiological and mechanical recapitulation [16], [17]. Manufacturing control at or below the level of cardiac bundles (50–100 μm low resolution) in cell patterning and over the microscale cell – material interface (i.e., cell-laden bioink [18]) facilitates the formation of biomimetic tissue structures which recapitulate the structural aspects of the in vivo myocardial phenotype. These networks can range from capillary micrometers to millimeter-sized vessels, followed by the composition's complexity (e.g., endothelial cells, smooth muscle cells, Fibroblasts, ECM) interfaces that should be hierarchically arranged, which should ideally be integrated with the required tissue models to be produced.
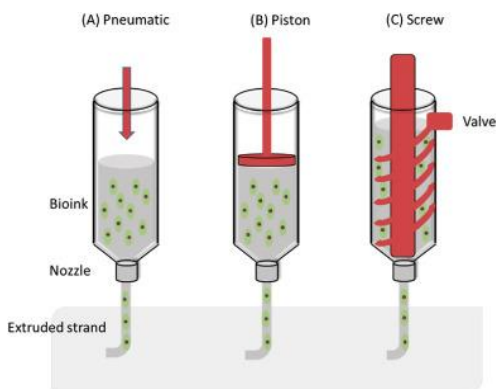
Figure 2. Extrusion based Bioprinting [19]

Their application can control ideal bioprinting resolution, but in most cases, it is identical to the most delicate features of tissue microarchitecture (for example, approximately 10 μm and a few hundred micrometers). It is often compared to the desired functions. Although cellular components reorganize within the ECM over time, higher resolution may be vital to reproduce the micro/nanoscale topography of ECMs in tissue models. It is desirable to consider the functional limitations of standard bioprinting techniques before designing and manufacturing micro-tissues [20]. In cell-laden bioinks, mechanical stresses on cellular components are minimized by lowering the bioink viscosity or increasing the nozzle's size and, therefore, hindering the final desired resolution. Bioprinting is used to develop the supporting structure and microfluidic channels for direct circulation of fluid, in addition to the hosted micro-tissue. The resolution also plays a crucial role in the constructed chip platform [21], affecting the various bioprinting process parameters and regulating the effective resolution [22].

Extrusion Bioprinting is based on pressure or plunger that pushes out a hydrogel (bioink), which has biomaterials and cells [23] (**Figure 2**). In this method, viscous bioinks

are deposited onto a substrate for creating 3D tissue constructs [20]. It is efficient in extruding high densities of cells, and it is required to accelerate tissue growth [24]. This method's damaging effects are a shear force on cellular components that leads to less viability and functionality [25]. A perfect bioink should have properties such as shear-thinning that minimizes bioink resistance under shear flow, and it must reestablish its physical properties reasonably rapidly after deposition [94] .

Over the different physical properties of bioinks, dynamic viscosity has a crucial role in bioprinting resolution and the printing threshold (i.e., beginning of bioink ejection from the nozzle and stable deposition on the surface) [92]. Extrusion bioprinting deals with a wide range of viscosities from 1×10^2 to 1×10^9 mPa.s [26]. Bioinks such as PEG polymers, hyaluronic acid, and alginate have been used to prove extrusion bioprinting's efficiency in producing tissue models [27]. The essential factor in bioprinting resolution is the velocity of the bioink inside the nozzle, caused by the pneumatic pressure or plunger speed [94]. It has been stated that cell viability also affects the flow rate; for example, a flow rate of 0.5 $mm^3 s^{-1}$ was found to be ideal for cell viability during the extrusion period. Cell viability and shear stress on the cells were the two governing factors considered [28].

1.3. Light-Assisted Bioprinting

Some other bioprinting methods are known as optical lithography or UV lithography. Photolithography is relatively more straightforward at the micron scale in creating the structure of any desired shapes rapidly and effectively[93]. However, the traditional photolithography is intrinsically limited by the wavelength of the light used and the typical resolution generated in laboratories, going down to 100 nm. With high-intensity

ultraviolet light, it is possible to decrease the feature sizes to 50 nm [29]. In SLA, the ultraviolet (UV) laser is directed to a vat of photopolymer resin [4]. The UV laser is used to draw a pre-programmed design or shape onto the surface of the photopolymer vat with the help of computer-aided manufacturing or computer-aided design (CAM/CAD) software [30]. Photopolymers are responsive to ultraviolet light, such that the resin is photochemically solidified and forms a single layer of the desired 3D material [31]. Then the build platform dampens one layer, and the wheel coats the top of the tank with resin [32]. This process continues for each design layer until the 3D object is fully completed (**Figure 3**). The final parts must be treated with a solvent to clear the wet resin from their surfaces. It can print "bottom-up" parts with the help of a vat with a transparent bottom and by focusing the UV or deep-blue polymerization laser upwards through the bottom of the vat. The inverted stereolithography machine starts printing by bringing down the build platform to touch the bottom of the resin-filled vat, and then it constantly moves the height of one layer. The UV laser then writes the bottom-most layer of the desired part through the transparent bottom of the vat. Then the vat is "rocked," flexing and tearing the bottom of the vat away from the strengthened photopolymer. The toughened material detaches from the bottom of the vat and remains attached to the rising platform while the new liquid photopolymer runs from the ends of the partially constructed portion. The UV laser then writes a second-from-the-bottom layer and repeats the process. The great benefit of this bottom-up mode is that the build volume can be much significantly larger than the vat itself, and just enough photopolymer is required to hold the bottom of the build vat continuously full of photopolymer [32].
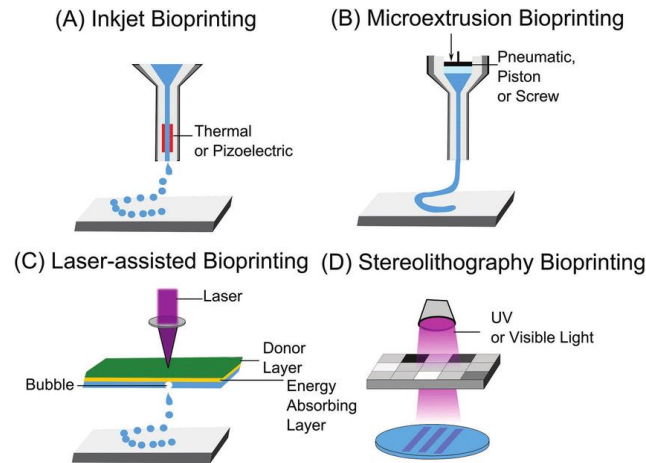
Figure 3. Various types of Bioprinting methods [33]

1.4. Bioinks

Bioinks are materials that contain living cells and biomaterials that mimic the extracellular matrix environment and are used for printing artificial living tissue. Hydrophilic gels are generally referred to as hydrogels, are networks of polymer chains that are sometimes found as colloidal gels in which water is the dispersion medium [34]. Hydrogels are polymeric materials that absorb water and swell, forming network chains. The carrier material is usually a biopolymer gel-like hydrogel, which acts as a 3D molecular scaffold. Cells attach to this gel, and this enables them to spread, grow, and increase. A fully swollen network can contain nearly 99% water [35]. The water-retaining ability of hydrogels is due to the functional groups such as hydroxylic (-OH), carboxylic (-COOH), acidic (-CONH-), primary amidic (-CONH_2) and sulphonic (SO_3H) groups found in the polymer network [36]. There are various uses of hydrogels in biomedicine, pharmaceuticals, materials science, food science, etc. Their features, mainly related to their

ability to transport solvents (water)/active molecules (e.g., drugs or nutrients), and their mechanical resistance determine their use.

Natural Hydrogels: Natural hydrogels are of natural origin and are prepared using natural polymers such as proteins and polysaccharides like alginate, chitosan, and dextran [37], [38]. They can form swollen 3D networks that give them the ability to diffuse molecules and cells. Nonetheless, they are similar to natural soft tissue, which is excellent for biomedical applications [39]. The common biomaterials include collagen, silk fibroin, hyaluronic acid, chitosan, alginate, and hydrogels derived from decellularized tissues. Natural hydrogels' unique properties include biocompatibility, biodegradability, low cytotoxicity, the possibility to tailor the hydrogel into an injectable gel, and their similarity to the physiological environment.

Synthetic Hydrogels: Synthetic hydrogels are of synthetic origin and are synthesized via chemical polymerization using humanmade polymers and homopolymer, copolymeric, and multipolymer. Poly(ethylene glycol)-polylactide-poly(ethylene glycol)-based hydrogel is an example for synthetic hydrogel [40].

Hybrid Hydrogel: The combination of both the synthetic and natural polymer form a hybrid hydrogel. 2-hydroxypropyl meth acrylamide is an example of a hybrid hydrogel.

1.5. Numerical Modeling

Many applications are too complex and cannot be solved using mathematical problems with exact formulas or analytically. Numerical modeling uses mathematical models to describe the physical conditions of fluid-like materials using numbers and equations. Partial differential equations help find the solution, but it is difficult to solve

them directly. Apart from mathematical methods, the most used numerical method is the finite element method that provides approximate solutions for these equations. A general numerical model generally consists of four components, followed by a flow chart (**Figure 4**).
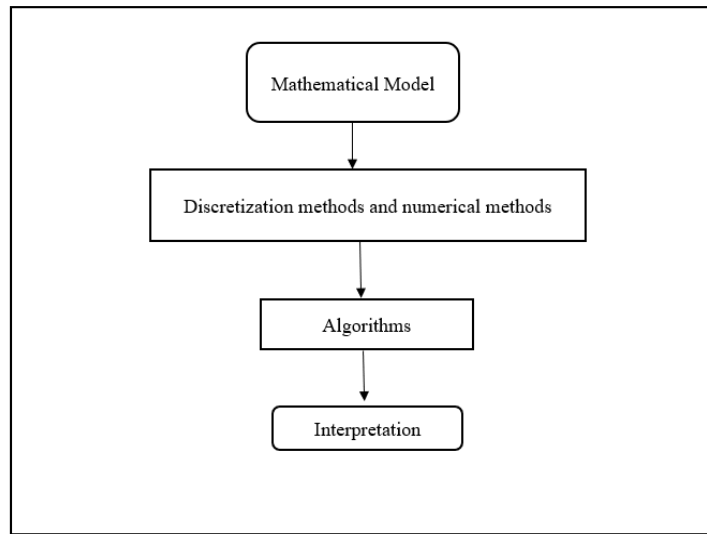
Figure 4. Steps in Numerical Modelling [41]

A mathematical model is a quantified description of a system of fluid problems such as boundary conditions and governing equations. The governing equations are generally partial differential equations [42]. Hydrogels are categorized as fluids due to their multiphasic property in which multiple components co-exist (water, polymer, etc.) [43]. The discretization methods and numerical methods convert the mathematical models' governing equations to discrete equations [44]. These discrete equations can approximate

the solution of the governing equations. The finite element method, finite difference method, or finite volume method subdivides an object into smaller pieces (element), creating a mesh. The discrete equations are solved numerically by each component [44].

Algorithms: Algorithms are computer programs that approximate the solution using the concept of numerical methods described above. Algorithms can be represented in many forms of notation, including natural languages, pseudocodes, flowcharts, drakon-charts, programming languages, or control tables (processed by interpreters). Standard algorithm expressions tend to be lengthy, unclear, and are rarely used for complex or technical algorithms. Pseudocode, flowcharts, drakon-charts, and control tables are structured ways to express algorithms that avoid many ambiguities common to natural-language statements. Programming languages are mainly utilized to illustrate algorithms in a manner that can be implemented by a computer but are also frequently used to describe or record algorithms. Algorithm design refers to the technique or mathematical process used for problem-solving and engineering algorithms. The algorithms' design is part of several functional studies' solution theories, such as dynamic programming, split, and conquest. Techniques for the design and implementation of algorithm designs are also referred to as algorithm design patterns; some examples include template method pattern and decorator pattern.

Typical steps in the development of algorithms: [45]

1. Problem definition

2. Development of a model

3. Specification of the algorithm

4. Designing an algorithm

5. Checking the correctness of the algorithm

6. Analysis of algorithm

7. Implementation of algorithm

8. Program testing

9. Documentation preparation

Interpretations are made based on the solutions offered by the numerical models.

1.5.1. Finite element method. The finite element method (FEM) is mostly used to solve a wide range of engineering and mathematical models that include a wide range of traditional fields like structural analysis, heat transfer, fluid flow, and mass transport. It is a numerical method for solving the partial differential equations in two or three space variables, including some boundary value problems. FEM subdivides a larger system into smaller, simpler parts called finite elements, also called a mesh, to solve a problem. The numerical domain for the solution has a finite number of points. The finite element formulation of a boundary problem results in a set of algebraic equations. The method approximates the unknown function over the domain [46]. The finite elements are modeled using simple equations, which are then assembled into a larger system of equations that models the entire problem.

FEM is used to simulate the inks' fluid characteristic in the flow channels of the positive displacement 3D printers under different technological parameters (viscosity, relaxation time, inlet volume flow rate ratio and nozzle diameter) to provide a theoretical basis for 3D printing food materials [47]. Mechanical properties are defined and predicted

using the finite element method, but it is difficult to predict the interparticle collisions and forces. Other methods resolve this kind of difficulty.

1.5.2. Discrete element modeling. Discrete Element Modelling (DEM) is a numerical model used to compute a large number of small particles' motion and effects. DEM describes the mechanical behavior of the particles' assemblies in the form of discs and spheres [48]. The application of the DEM is to study the granular materials. DEM's importance has been demonstrated in various chemical engineering fields, pharmaceuticals, powder metallurgy, agriculture, and many others. DEM simulations have been extensively applied to diverse problems in granular processes, for example, the packing of particles [49] and the flow from a hopper [50].

DEM is used mainly for discontinuous approaches, and FEA is used for continuum approaches. The reason behind the evolution of DEM is the need to solve the rock mechanics problem. The DEM code takes advantage of parallel processing to scale up the material properties or lengthen the simulation. As a consequence, the average physical properties and effects are perceived as a continuum in the aggregate particles. In liquid-like or gas-like granular flux, the continuum method can treat the material as a fluid and use computational fluid dynamics. There are drawbacks to the homogenization of granular scale physics. DEM can be computationally expensive; therefore, either the simulation's size or the number of particles are regulated. These drawbacks are well-documented and should be considered carefully before attempting to use a continuum approach.

Particle Flow Code (PFC) released by Itasca Consulting Group, Inc., is a general-purpose DEM framework that includes a computational engine and graphical user

interface. The PFC simulates both 2D and 3D models. The general particle-flow model simulates the mechanical behavior consisting of a series of dynamically formed particles. The model consists of distinct particles that interact with each other. If the particles are rigid, this system's mechanical behavior is defined by the movement of each particle and the inter-particle forces acting at the points of contact. Newton's laws of motion provide a fundamental relationship between the motion of a particle and the forces that cause the motion (**Figure 5).** The force system may be in static equilibrium (in which case there is no motion) or permit the particles to flow. Suppose the particle-interaction law models physical contact between the particles. In that case, the contact behavior is characterized by a soft contact approach in which the finite normal stiffness is used to describe the stiffness that occurs at the contact point. The rigid particles can overlap in the vicinity of the contact point. More complex behavior can be modeled by allowing the particles to be coupled together at their contact points. A bond is broken when the inter-particle forces acting at a bond overcome the bond control and result in tensile forces developing between the particles. These bonded blocks' interactions are modeled, including the formation of cracks that might cause blocks to fragment into smaller blocks. The law on particle interaction can also be derived from potential energy functions and models of long-range interactions. The PFC provides a particle-flow model containing the following assumptions:

1. The particles are treated as rigid bodies.

2. The fundamental particle shape is a (disk with unit thickness in 2D; the sphere in 3D), denoted ball.

3. The clump logic supports the creation of rigidly attached (disks with unit thickness in 2D; spheres in 3D), denoted pebbles. Each clump consists of overlapping pebbles that act as a rigid body with a deformable boundary. Clumps may be an arbitrary shape.

4. Particles interact at pair-wise contacts by means of internal forces and moment. Contact mechanics are embodied in particle-interaction laws that update the internal forces and moments.

5. Behavior at physical contacts uses a soft-contact approach where the rigid particles overlap one another at contact points. The contacts occur over a vanishingly small area (i.e., at a point). The magnitude of the overlap and the relative displacement at the contact point are related to the force-displacement law's contact force.

6. Bonds can exist at contacts among particles.

7. Long-range interactions can also be derived from energy potential functions.

update particle + wall positions and set of contacts

Law of Motion
(applied to each particle)
• resultant force + moment

Force–Displacement Law
(applied to each contact)
• relative motion
• constitutive law

contact forces
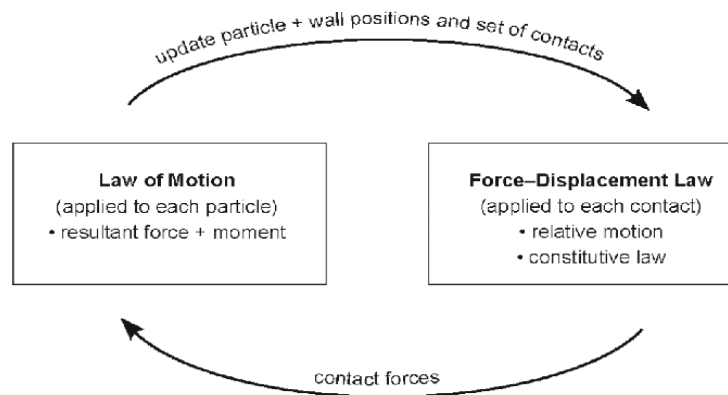
Figure 5. Calculation cycle in PFC^{2D} [51]

The assumption of particle rigidity is necessary when most of the deformation in a physical system is accounted for by the movements and interfaces. The deformation of a packed-particle assembly (or a granular assembly such as sand) is well-described by this assumption. The deformation primarily results from the particles' sliding and rotation as rigid bodies and the opening and interlocking at interfaces, not from individual particle deformation. Precise modeling of particle deformation is not necessary to obtain a good approximation of such systems' mechanical behavior. In addition to traditional particle-flow applications, PFC can also be applied to analyzing solids subjected to the prescribed boundary and initial conditions. In such models, the continuum behavior is approximated by treating the solid as a compacted assembly of small particles. Measures of stress and strain rate can be defined as average quantities over a representative measurement volume for such systems and estimate interior stresses for granular materials such as soils or solid materials such as rock or plastics formed by powder compaction. In addition to balls and clumps, the PFC particle-flow model also includes walls. Walls allow one to apply velocity boundary conditions to assemblies of balls or clumps for compaction and confinement. The balls, clumps, and walls interact with one another via the forces that arise at contact. The equations of motion are satisfied for each ball and clump. However, the equations of motion are not satisfied for each wall (i.e., forces acting on a wall do not influence its movement). Instead, the motion is specified by the user and remains constant regardless of the contact forces. Also, contacts may not form between two walls; thus, contacts are either ball-ball, ball-pebble, pebble-pebble, ball-facet, or pebble-facet.

Chapter 2

Discrete Element Modeling (DEM)

2.1. Introduction

DEM was first created by Cundall [52], [53] for analyzing rock mechanics problems. The basic formulation of DEM using spherical or cylindrical particles was later proposed by Cundall and Strack [54] to explore the constitutive laws for soil. Cundall and Hart [55] showed that DEM is better at modeling non-continuum material than numerical tools such as the finite element method. For example, FEM solves problems in continuum while DEM solves problems in discontinued media. The variation is that we should work with the restructuring, in compaction, of discrete elements of the soil matrix. But the boundaries understudy must be defined in finite elements and algorithms used for modelling in the DEM algorithm.

DEM assumes that the material can be shown as an assembly of rigidly interacting particles among themselves. The material's overall behavior is accounted for by the inter-particle mechanical contact law and the capillary attraction. The contact law can be discovered as the formulation of the material model on the microscopic level. The DEM coding software PFC^{2D} [51], [56] was implemented in this analysis to model the structural granular materials. PFC^{2D} follows an explicit time integration scheme to simultaneously solve Newton's equations of translational and rotational motion for all particles and the accuracy of the simulations is thus governed by choice of the contact force model. This chapter presents the formulation developed by Ma et al. [57].

2.2. Equations of Motion

The translational and rotational motion of rigid spherical or cylindrical particles is well-defined by the Newton-Euler equations of rigid body dynamics. For the i-th element, we can write the equations as

$$m_i \ddot{u}_i = F_i, \qquad (2.1)$$

$$I_i \dot{\omega}_i = T_i, \qquad (2.2)$$

where u_i is the displacement of the particle center in a fixed (inertial) coordinate frame $\mathbf{X}$, ω_i is the angular velocity, m_i is the element (particle) mass, I_i is the moment of inertia, F_i is the resultant force, and T_i is the resultant moment about the central axes. Vectors F_i and T_i are the sums of all the forces and moments applied to the i-th element

$$F_i = \sum_{c=1}^{n_c} F_i^c + F_i^{ext} + F_i^{damp} \qquad (2.3)$$

$$T_i = \sum_{c=1}^{n_c} (r_i^c \times F_i^c + q_i^c) + T_i^{ext} + T_i^{damp} \qquad (2.4)$$

where F_i^{ext} and T_i^{ext} are external loads, F_i^c is the contact force for the interaction with neighboring spheres and other obstacles, F_i^{damp} and T_i^{damp} are the force and torque resulting from the damping in the system (will be discussed in section 2.4), r_i^c is the vector connecting the center of the particles of the i-th element with contact point c, n_c is the number of particles being in contact, and q_i^c is the torque due to rolling or torsion (not related to the tangential forces).

The rotational equation (2.2) is valid for spheres and cylinders (in 3D). It is simplified to a general form for an arbitrary rigid body with the rotational inertial properties represented by the second-order tensor.

2.3. Mechanical Contact Forces

Once the contact between a pair of elements has been detected, the contact point forces are calculated. The contact forces represent the interaction between the two interacting bodies F_i and F_j ,which by the Newton's third law satisfy the following relation:

$$F_i = -F_j, \tag{2.5}$$

It is assumed $F = F_i$ and substitute F into the normal and tangential components, F_n and F_t, respectively (**Figure 6**)

$$F = F_n + F_t = f_n \mathrm{n} + F_t, \tag{2.6}$$
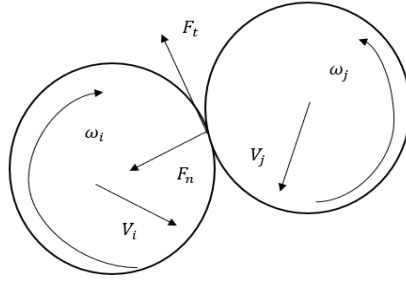
Figure 6. Decomposition of the contact force into the normal and tangential components.

Where n is the unit vector normal to the particle surface at the contact point (indicates that it lies along the line connecting the centers of the two particles) and pointed outwards from the particle *i*.

$$n = \frac{x_j - x_i}{\|x_j - x_i\|},$$ (2.7)

The contact forces f_n and F_t were calculated using a constitutive model formulated for the contact between two rigid spheres (or discs in 2-dimensional) (**Figure 7**).

The contact interface in our formulation is calculated using the normal and shear contact stiffness k_n and k_s [F/L], respectively, the Coulomb friction coefficient μ, and the normal and shear damping coefficient η_n and η_s [F/(L.T^{-1})].
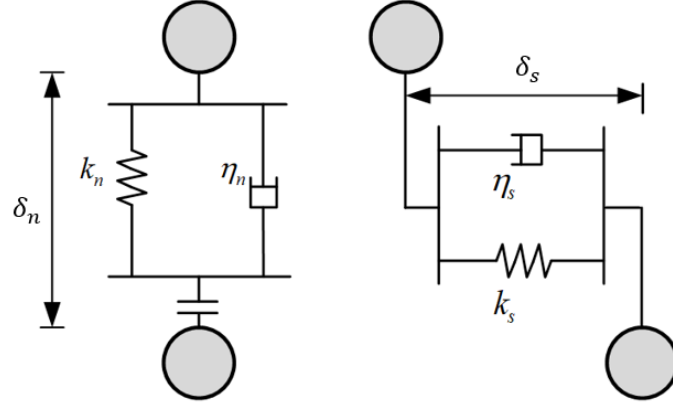
Figure 7. Schematic representation of particle interactions in the mechanical contact model: (a)   normal (b) shear [57].

All the microscale parameters are not explicitly observable, and it is more convenient to define the suitable material properties as input parameters instead. Hence, the normal contact stiffness is determined from,

$$k_n = 2E_c(R_a + R_b), \tag{2.8}$$

where E_c is the apparent modulus for the particle-particle contact; and R_a and R_b are the radii of the two particles in contact. The contact model relates the contact forces and particle overlap, assuming they are positive,

$$F_n = k_n\delta_n + \eta_n\delta_n \text{ , and } \quad \Delta F_s = k_s\Delta\delta_s + \eta_s\delta_s \text{ ,} \tag{2.9}$$

Coulomb's law of friction is followed,

$$F_n \leq \mu F_s \text{ ,} \tag{2.10}$$

where F_n and F_s represent the normal and shear contact forces, respectively; δ_n is the overlap ($\delta_n < 0$ indicates the gap at the contact) and δ_s is the slip between the pair of

particles. The normal and the tangential damping coefficients, η_n and η_s Are material constants related to the mass, stiffness, and coefficient of restitution (COR). Normally, the COR is determined by the experiments, and thus,

$$\eta_n = 2\beta_n\sqrt{m_C k_n}, \text{ and } \eta_s = 2\beta_s\sqrt{m_C k_s} , \qquad (2.11)$$

where m_C is the effective inertial mass of the contact; β_n and β_s are the ratios of damping constant and the critical damping constant, respectively. Critical damping ratios can be calculated in terms of the COR according to [58],

$$\beta = -\frac{\ln(COR)}{\sqrt{(COR)+\pi^2}} , \qquad (2.12)$$

Normally COR ranges from 0 to 1, whereas 0 indicates the particle collision is highly elastic, and 1 indicates the particle-particle collision is highly inelastic. When the working material is very soft, then particle-particle collision must be elastic and must not be highly elastic, so we assume COR = 0.1 and $\beta_n = 0.59\ kg\ /\ m \cdot s$. For simplicity, we assume $\beta_n/\beta_s = 1.0$.

The linear elastic spring and dashpot model is responsible for the mechanical forces, including the normal, shear, and viscous damping forces. However, this model becomes problematic if significant nonlinear behavior or large overlaps are present. In this analysis, particles are subject to gravitational body force and boundary traction only, which means the inter-granular overlaps are less than 0.5 percent of the mean grain radius. Therefore the particle surface gap must be 0.5% of the mean grain radius for better flowability. The flowability of the particles is negligible under the impact of the overlapping conditions [59].

2.4. Capillary Forces

The cohesive force assigned to moisture is considered by applying a capillary bridge model, see **Figure 8**. Generally, the capillary forces consist of several components, of the two most significant contributions, which are surface tension and meniscus capillary suction [60]–[62]. Making a cross-sectional cut at the neck of the liquid bridge (marked as A- A'); the total capillary force can be expressed as,

$$F_{cap}=2\pi y_0 \gamma + \pi y_0^2 \Delta p \qquad , \qquad (2.13)$$

Where γ is the surface tension of the liquid, Δp is the capillary suction pressure, and y_0 is the neck radius of the liquid bridge, see **Figure 9**. As per the theory, capillary force is the function of the liquid bridge parameters, including liquid volume V_b, gap δ_n (negative value), liquid surface tension γ, and particle-liquid contact angle θ. By solving Laplace-Young equations, the research solution of the capillary force can be reached [60], [63]–[66]. These equations can be solved by using the iteration for the given values of δ_n and V_b [63], [67]. While computational power and advanced mathematical algorithms have been enhanced to deal with complex computational problems, particularly for DEM simulations, simultaneous equation systems have been solved at each point of contact until it is ineffective. Hence, an explicit expression of the capillary force is required.
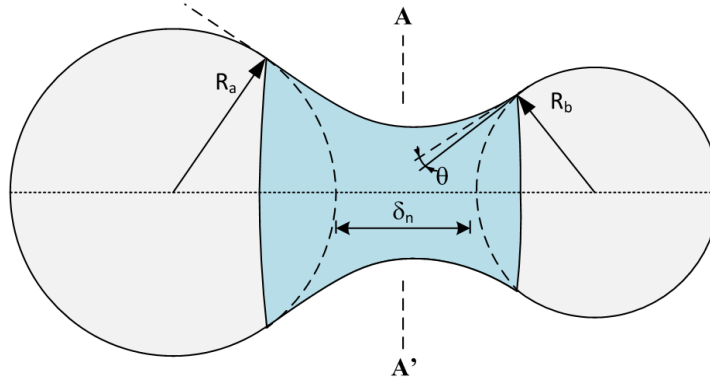
Figure 8. Capillary bridge model, A- A' shows the neck of the bridge.

Numerous numerical models have been proposed to solve the liquid bridge's capillary force [68], [69]. Mikami et al. [65] presented an expression for monodisperse particles. Soulie et al. [70] widened their work to account for polydisperse cases by fitting the numerical solution from Eq. (2.13). The capillary force will then be represented with contact geometries and properties of the liquid bridge.
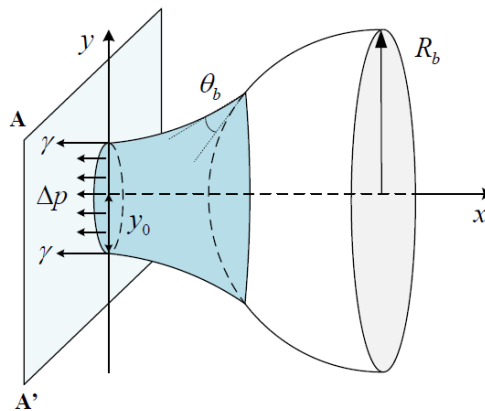
Figure 9. Capillary suction and surface tension in the liquid bridge at the cross-section A-A'.

$$F_{cap} = \pi\gamma \sqrt{R_a R_b} \left[exp\left(a\frac{\delta}{R_a} + b \right) + c \right], \tag{2.14}$$

Where $\delta = (-\delta_n)$ is the distance among the particle and a, b and c are constants defined as,

$$a = \text{-}1.1 \left(\frac{V_b}{R_a{}^3} \right)^{-0.53} \;,$$

$$b = \left(-0.148ln\left(\frac{V_b}{R_a{}^3} \right) - 0.96 \right)\theta^2 - 0.0082ln\left(\frac{V_b}{R_a{}^3} \right) + 0.48 \;, \tag{2.15}$$

$$c = 0.0018 \, ln\left(\frac{V_b}{R_a{}^3} \right) + 0.078,$$

Note that R_a is the radius of the larger particle in the contact pair. The explicit analytical solution in Eq. (2.7) and (2.8) are easily implemented into DEM to determine the capillary force if liquid bridge volume, contact angle, and separation distance at contact are given. The capillary force reaches the maximum when the particles are in contact. Later, it starts to decline as the separation increases. The liquid bridge is assumed to be stable as $\delta<\delta_{max}$. Rupture occurs when $\delta > \delta_{max}$. The maximum stability distance δ_{max} has been examined in [64], [71]. The results represent that the rupture distance is proportional to the cube root of the liquid volume if $\theta \leq 2\Pi / 9$,

$$\delta_{max} = (1 + 0.5\theta)V_b^{\frac{1}{3}}, \tag{2.16}$$

Therefore, the overall cohesive capillary force between two particles can be expressed as,

$$F_{cap} = \begin{cases} F_{max} & \delta_n \geq 0 \\ \pi\gamma \sqrt{R_a R_b} \left[exp\left(a\frac{\delta}{R_a} + b \right) + c \right] & 0 \leq \delta_n \geq \delta_{max} \\ 0 & \delta_n < \delta_{max} \end{cases} \tag{2.17}$$

2.5. Liquid Bridge Volume

According to Eq. (2.17), the contact angle θ and liquid bridge volume V_b to calculate the capillary bridge force is required. For simplicity, it is assumed that the contact angle is small enough that $\theta \simeq 0$. Thus it is important to define an explicit expression to calculate V_b at each contact. This study assumes the liquid within the granular system is uniformly distributed and associated with each particle. The liquid migration among the particles is negligible. When a liquid bridge is created, the bridge's total volume is calculated according to the total particles and the number of contacts (liquid bridges) each particle has. All the liquid inside the assembly is fully distributed either in the liquid bridge form or as free fluid if that particle does not have any active contacts. We define the ratio of liquid or free fluid when that particle does not have any active contacts. We define the ratio of the liquid volume to the solid volume as water content ω_c. Based on the definition of volumetric water content, the total liquid volume V_L becomes,

$$V_L = \omega_c . V_s \tag{2.18}$$

where V_s is the total volume of the particles. Based on our assumptions of liquid volume conservation law, the total volume of the liquid associated with particle R_i can be calculated as,

$$V_{L,i} = \omega_c \frac{4}{3} \pi R_i^3 \tag{2.19}$$

Assuming this particle has n active contacts with adjacent particles, the liquid bridge volume between particle R_i and R_j can be resolved using,

$$V_{b,i\leftrightarrow j} = \frac{4}{3} \pi \omega_c \left(\frac{1}{n} R_i^3 + \frac{1}{m} R_j^3 \right) \tag{2.20}$$

If a particle doesn't have any contact with adjacent particles or boundary walls, the liquid associated with particles won't generate liquid bridges. Since we primarily analyze the effect of humid air on granular materials' flowability, during this study, the entire moisture content within the system is considerably low. Therefore, it is rational to assume that a liquid bridge is made only after two particles are strictly in touch and neglecting the absorption effect in liquids.

2.6. Macro-Micro Humidity Conversion

In this model, we need to calculate the microscale moisture content to determine the capillary force. In experiments, the relative humidity of the air is considered constant at room temperature. Hence, we will derive an expression for microscale moisture content as a function of macroscale relative humidity.

Relative Humidity (RH) is defined as the ratio of the partial pressure of water vapor to the equilibrium vapor pressure of water at a given temperature:

$$\text{RH} = \frac{e}{e_\omega} \tag{2.21}$$

where e is the vapor pressure and e_ω is the saturated vapor pressure. By rearranging Eq. (2.21), the vapor pressure can be calculated as:

$$e = \text{RH} \cdot e_\omega \tag{2.22}$$

e_ω is a function of temperature t that can be expressed using the so-called August-Roche-Magnus approximate empirical solution to the Clausius-Clapeyron equation [72], [73]

$$e_\omega(t) = 0.61094 \, exp \, (7.625t \, / \, (t + 243.04) \,) \tag{2.23}$$

In Eq. (2.23), temperature t is in degrees Celsius($°C$) whereas e_ω is in KPa. By the laws of idea gas equation [74], [75],we have,

$$eV = n_m \xi R_v T \qquad (2.24)$$

where V is the total volume of one mole ($n_m = $ 1mol) air, R_v is the specific gas constant for water vapor ($R_v = $ 461.5 J/kg. K)), T is the temperature in Kelvin (K), and ξ is the molar mass of water vapor ($\xi = $ 18.02 g/mol). The absolute humidity (AH) is defined as the moisture per cubic meter of air. From Eq. (2.25), we have,

$$AH = \frac{n_m \xi}{V} = \frac{e}{R_v T} = \frac{RH.e_\omega}{R_v T}, \qquad (2.25)$$

For a given particle assembly, we can indicate a relative humidity and porosity υ. Then the water content ω_c can be determined as

$$\omega_c = \frac{V_L}{V_S} = \frac{\upsilon}{1-\upsilon} \cdot \frac{AH}{\rho_\omega}, \qquad (2.26)$$

where ρ_ω is the liquid density. Now substituting Eq. (2.25) into Eq. (2.26), the relationship between RH and ω_c can be expressed as,

$$\omega_c = \frac{\upsilon}{1-\upsilon} \cdot \frac{RH.e_\omega}{R_v T \rho_\omega}, \qquad (2.27)$$

Using the above equation, we can convert the relative humidity to microscale water content, which is used as an input parameter for the numerical model.

2.7. Van der Waals Forces

In addition to the capillary force, the Van der Waals force becomes a crucial factor that governs the flow behavior of dry and wet powders [76]–[78]. The concept of applying the Van der Waals force to wet powders was utilized in this project to regulate the flow

behavior of hydrogel. Van der Waals forces are electric dipole forces generated by the electron cloud and the nucleus; they operate in all matter and are sensible for the attractive force between the molecules.
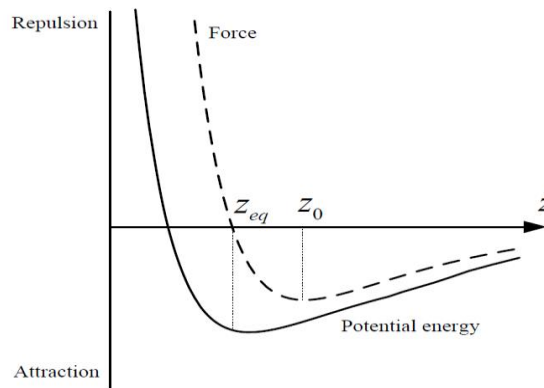
Figure 10. Potential energy and force between two molecules.

Usually, these are weak forces and negligible when studying the macroscale properties of materials. However, the grain size of the hydrogel investigated in this study can be as small as several micrometers. Van der Waals's magnitude becomes comparable to the inter-particle contact force caused by gravity as the particle size reduces. As the particle flow is mostly triggered by gravity, it is generally solved during the repose angle test. Hence, these weak forces affect the flowability of the particles as a function of particle size.
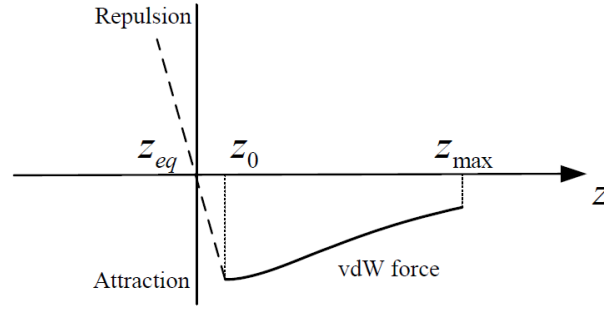
Figure 11. Interaction forces between the two particles.

A simple mathematical model can describe interactions between the two particles, the Lennard-Jones potential $U(z)$, see **Figure 10**. The interaction force can then be calculated using the derivative of the potential energy equation. The analytical solution of the interaction potential [79] is complex and computationally expensive. So the particles in our analysis are sufficiently large compared to the size of the molecules that Van der Waals force simplifies to [80]:

$$F_{vdW}(z) = \frac{AR_{eq}}{6z^2},$$ (2.28)

Where A is the Hammaker coefficient considered as a material constant ($A\epsilon$ $(10^{-19} \sim 10^{-20})$), R_{eq} is the equivalent particle radius as previously defined, and z is the shortest distance between the particle surfaces.

The force calculated from Eq. (2.28) becomes problematic when the distance z is approaching zero. This issue has been addressed in the literature by implementing a minimum cut-off distance [81]–[83]. In existing models, the attractive forces remain constant when it is within the cut-off distance. This assumption is inaccurate when investigating flowability issues because it overestimates the particle overlaps closely

related to particle flow behaviors. This discrepancy is critical, especially in "soft contact" models [54], where the contact forces stem from particle overlaps. Hence, we assume that the equilibrium state where the attraction is balanced by repulsion is obtained at $z_{eq}= 0$, as shown in **Figure 11**. The attractive force linearly reduces to zero when the separation distance is within z_0. The shape of total inter-particle forces is thus comparable to the forces between real molecules (the dashed line shown in **Figure 10**).

With the hypothesis of $z_{eq}= 0$, the interaction force becomes zero if two particles are in perfect contact state (no gap or overlap), the maximum attractive force is obtained at $z = z_0$, defined as the cut-off distance. The experimental results of the Van der Waals forces between two half-spaces suggest that the equilibrium distance is roughly between 1^{-5}Å (1 Å $= 10^{-10}m$) and the cut-off distance is $z_0 = 1.2\, z_{eq}$ [84]. However, these experimental results cannot be applied directly in this model because the formulation of Van der Waals forces is different in particle-particle contact. Additionally, no attempt has been made in this study to simulate the actual molecule nor the electron cloud. Therefore, the cut-off distance reported in the literature is not comparable to z_0 in DEM. We consider z_0 , the parameter that needs to be calibrated according to the behavior of steel powder. The Van der Waals force drops off quickly as the particle separation increases. To speed up the simulations, we set a maximum break down distance, $z_{max} =$ Req/4, which the interaction force reduces to zero. Considering that z_0 is normally in nanometer-scale while particle size in this study is in micrometer scale, the ratio of force at break down distance to the force at a cut-off distance is about O (10^{-7}). It is thus safe to neglect the interactions when $z = z_{max}$ without influencing the macroscale behavior of particles.

(a) $z_0 = 0.5$ nm

(b) $z_0 = 1.0$ nm
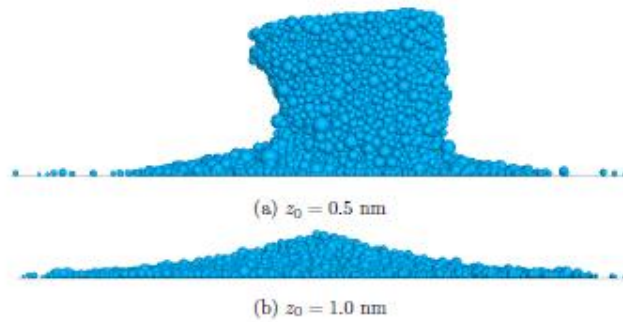
Figure 12. Effect of cut-off distance z_0 on the flowability of fine powders [57].

Normally, a calibration process is conducted to determine the powder's cut-off distance, which was experimentally done [57] through the repose test. The numerical simulations of repose tests are performed with a particle assembly to qualitatively show the effect of the cut-off distance on the flowability. The cut-off distance is set to be $z_0=0.5$ nm and 1.0 nm, respectively shown in **Figure 12**.At $z_0=0.5$ nm, the cohesion attributed to Van der Waals force is so significant that the particle clump had failed to flow, while when z_0 is increased to 0.5 nm, the particles exhibit a good flowability.

Hence, the forces such as mechanical forces, capillary forces, and Van der Waals forces are all implemented in a user contact model at the ball-ball and ball-facet contacts. The model is named by the smart-lobo contact model that determines the mechanical behavior of a PFC model. The mechanical force parameters which influence the smart-lobo contact model are,

Particle density (ρ): Density of the hydrogel(or any material) used as an input at the contact that defines how dense the material would be in the numerical model.

Particle radius(r): Particle(Ball) size used in the model. The convergence study was later discussed in the next chapter, including how the particle size affects the model strength.

Elastic modulus(E): The mechanical properties of the actual material have been imparted as input to the contact model, influencing the PFC model's material behavior.

Stiffness ratio (k_n / k_s): The ratio of normal and shear stiffness affected by the elastic modulus and impact the contact's strength in both normal and tangential direction.

Damping ratio (β): The constant value affects the contact model's viscosity and is calculated according to the COR mentioned in eq 2.12.

Friction coefficient (μ): A small amount of force that restricts the contact overlaps between the particles during an impact load and is applied externally, explained in eq 2.10.

Along with the mechanical force parameters, capillary force, and Van der Waals force, the parameters each have a role in the model. Still, the influence is very minute due to the very tiny scale modeling. However, to maintain the particles together and always make a rigid geometry, we retain the moderate cut-off distance(z_0).

The individual parameters' values are detailed in **Table 1** and **Table 2**, some are experimental, and some are determined based on the equations listed above. The effect of each parameter will be discussed later in the parametric analysis.

The next chapter discusses the methodology that includes the calibration study considering experimental research on the hydrogel's uniaxial compression test.

Chapter 3

Methodology

3.1. Introduction

A study conducted based on the set of microscopic parameters calibrated using the experimental data of a conventional bioink: the alginate-gelatin-based hydrogel. The PFC method has been used to model the hydrogel's behavior in 2D [56], and encouraging results have been obtained. This study is carried out by first collecting the basic physical and mechanical properties of the material extracted from the results of uniaxial compression. Then a numerical model that mimics the microstructure of the hydrogel is generated in PFC^{2D}. After that, a set of microscopic parameters are determined so that the numerical results match the measured mechanical properties. Finally, the calibrated microscopic parameters are utilized to systematically study the effect of parameters and determine the interparticle forces between the particle microstructure in PFC^{2D} during the extrusion of hydrogel.

3.2. Model Genesis

The numerical simulation operation system is Windows 10 (on a personal computer with an Intel Core i7,3.30 GHz CPU and 16 GB RAM). The PFC^{2D} version 5.0 was adapted to run on Windows and was used to simulate the hydrogel. To do PFC simulations, first a PFC^{2D} a model consisting of densely packed spheres (particles) bonded together needs to be generated and the particles' microscopic properties and the bonds assigned. There are two types of sphere packing methods: geometric method and dynamic method [85].The dynamic packing method is commonly used in PFC^{2D} simulations because it is

available as a standard PFC^{2D} function in FISH Tank [56]. The FISH function has been used by Itasca since PFC^{2D} was released and helped users apply PFC^{2D} easily to solid based simulations. After years of development, the FISH Tank has evolved to a collection of powerful functions and routines to generate, view, monitor and analyze DEM results under different boundary conditions. In this study, we deployed the dynamic method of packing to generate the standard PFC^{2D} specimens.

The model genesis procedure in PFC^{2D} includes four steps **(Figure 13):**

1) Generate the particles randomly with diameters in a specified range within a geometry bounded by frictionless walls.

2) Adjust the system by allowing particles to move under zero friction until the mean stress is near (or static equilibrium is obtained). This step eliminates the large overlaps and provides an isotropic state.

3) Install low isotropic stress by applying the gravity between particles simultaneously.

4) Particles must have less than three contacts iteratively so that these particles have at least three contacts, and their mean contact normal force is low with the mean contact force of the assembly.
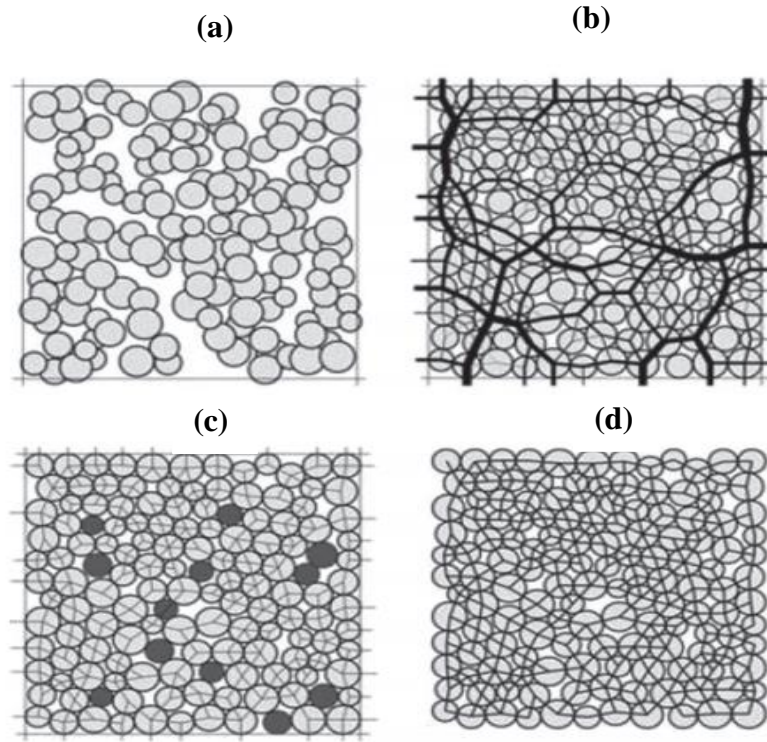
Figure 13. Material genesis procedure: (a) Particle assembly after initial generation but before rearrangement; (b) contact force distribution after second step; (c) floating particles and contacts after second step; (d) Contact-bond network [51].

It must be noted that the target porosity of the compact particle assembly used in PFC^{2D} is set to 35%, which is the theoretical highest density that can be achieved for mono-sized particle close packing [86]. The total number of particles is generated upon the target porosity. The final porosity is then adjusted when applying isotropic stress under gravity. For particles following a uniform size distribution with diameters in the range[d], the total number (N) of particles that can be generated to fill a given volume V, at a given porosity n, can be determined by [56]

$$N = \frac{4V(1-n)}{\pi d^2} \quad\quad (3.1)$$

3.3. Experimental Test

3.3.1. Materials. The pore skin gelatin is 5% w/v of 1g, and low viscous alginate is 5% w/v of 0.6g, DPBS (Dulbecco Phosphate Buffer Solution).
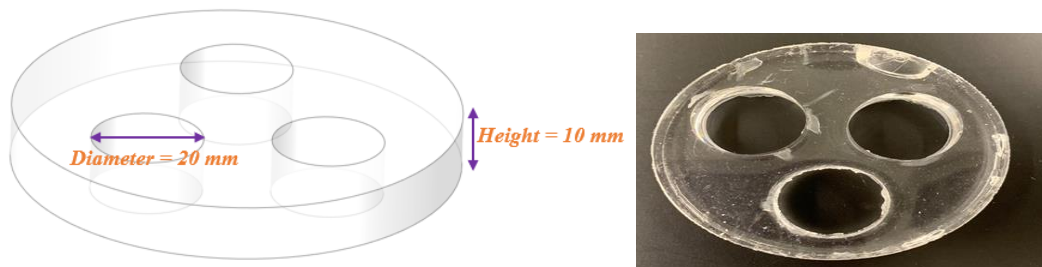
Figure 14. PDMS mold used for molding

3.3.2. Preparation of hydrogel. The preparation of the hydrogel sample has been described elsewhere [87]. In brief, 5% w/v of 1 g gelatin and 5% w/v of 0.6 g of low viscous alginate mixture was dissolved in 90ml of DPBS (Dulbecco Phosphate Buffer Solution). The resulting dispersion is stirred (using an overhead stirrer at 100 ± 5 rpm) at 70°C for half an hour until the mixture becomes a gel. The thick dispersion medium is then transferred in a mold to achieve the required density, as shown in **Figure 13**. Then the medium is converted into a membrane by the conventional casting method. The resulting membrane is stored in a dissector at 37°C. Model samples are cylindrical, with a diameter of 20 mm and a height of 10 mm, as shown in **Figure 14** and **Figure 15**.

38

Figure 15. Specimen used for compression

3.3.3. Compression testing. Uniaxial compression tests are performed on a custom-built machine (Shimadzu EZ-SX, Columbia, MD, USA) (**Figure 16**) at a loading rate of 0.1mm/s with a 100 N load cell. Samples are then blended for the test. The upper and the lower sample surfaces are fixed to the compression tester's platters to ensure that there will not be any slipping during the tests. We use the initial linear slope of the stress-strain curve between 0 and 0.1 strain to calculate the initial compressive modulus, where taken from the nominal stress-strain curve. Although the material's overall behavior is non-linear, the initial region is approximately linear, hence our analysis of this section to determine the modulus. The apparatus used in the experiment are shown in **Figure 15**.

The mechanical properties derived from the compression test are then compared with the numerical analysis data and hence calibrated to prove that the numerical model is valid for the purpose.

Figure 16. Compression Testing Machine

3.4. Proposed Hydrogel Model Using PFC^{2D}

The geometry of the numerical model was set up similarly to the experimental setup. The sample was generated with walls and balls where walls act as boundary conditions and balls as the materials. Initially, an unbonded assembly with the null model was assigned to every contact. The sample was 20 mm in length and 10 mm in height, conforming to typical laboratory core samples in 2D. The walls extended past the edge of the sample to allow variations in the sample size during loading. The null model was used because all the required parameters influencing the model were set to zero under the consolidation to maintain the system equilibrium in the geometry. The material properties were then assigned according to the experiment data represented in **Table 1** by implementing the smart-lobo contact model. Hence the properties are calculated based upon the particle radii. The sample is shown in **Figure 17**.
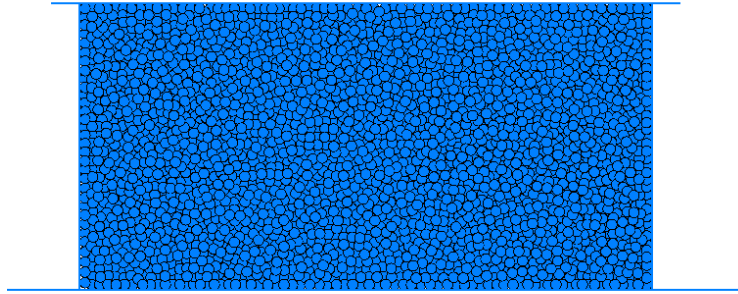
Figure 17. Randomly generated particles in a specified geometry

3.5. Convergence Study

The DEM study has examined various studies on the grain size for different materials through the single crystal properties [88]. Polycrystalline models have a lot of potential because the fabrication methods such as bioprinting produce polycrystalline microstructures. This investigation was based on the influence of the Youngs Modulus's grain size to observe a Hall-pitch effect. From these studies, there is agreement on the grain size behavior regarding the Youngs Modulus. As the grain size increases, the Youngs modulus increases. However, the UCS has shown decreasing behavior as the grain size increased, satisfying the Hall-Petch effect [88].

In this study, we investigated mechanical properties such as Youngs Modulus for different grain sizes. We performed compressive deformation for the hydrogel for the polycrystalline model in 2D and obtained the mechanical properties' grain size behavior. For a given model of specific grain size (ranging from 1000 µm to 100 µm), Young's modulus is derived at the elastic limit, i.e., approximately around 1% of strain. The method includes a geometry mentioned in section 3.3, where the uniaxial compression test is

conducted. The results are compared at different particle sizes aiming to observe whether the compression strength has been affected by the grain size, which further restricts the standard particle size for various applications.

3.6. Uniaxial Compression Test and Calibration

In this study, we investigate the effect of moisture and microstructural interactions by using synthetic granular material. Since our main concern is to calibrate the macroscale properties used in the smart-lobo contact model with the natural material, we generate a random number of particles, approximately 2228 particles, to replicate the hydrogel material each simulation within the domain.

It has been proved that the flowability of the granular materials is inversely proportional to the capillary force while the capillary force increases with equivalent particle size [89]. A limited number of particles are used to show the effect of capillary force on the macroscale's flowability inside the geometry. The average particle size is considered to be 200 microns. With smaller particles, the capillary force is significantly comparable to the contact forces stemming from gravity. We need a more extensive domain to show the transition in particle flow behaviors.

Table 1

Particle size and microscale parameters

Properties	Symbols	Values
Particle Density (kg/m^3)	ρ	1140
Particle radius(m)	r	0.0002
Elastic Modulus particle (MPa)	E	0.0039
Local damping ratio	β	0.5
Coefficient of restitution particle-particle	COR	0.1
Static friction coefficient particle-particle	μ	0.001
Normal to shear stiffness ratio	k_n / k_s	0.5
Cutoff-distance(nm)	z_0	0.5

Considering the computational cost, an optimal domain size that consists of approximately 2228 particles is chosen. The particle size characteristics, as well as microscale parameters, are listed in **Table 1.** In this study, liquid water is not explicitly simulated in the DEM framework. Instead, the moisture's effect is realized by exerting capillary forces at the particle contacts, by adjusting the water content or relative humidity, which is essentially equivalent, the capillary force changes accordingly. The environmental conditions and water properties are summarized in **Table 2.** These parameters apply to simulations of Uniaxial Compression tests in this study. The values displaced are from the parametric study during the analysis, discussed in the latter part of the chapter.

Table 2

Environmental conditions and water properties

Properties	Symbols	Values
Density (kg/m^3)	ρ	1000
Water surface tension(N/m)	γ	0.072
Temperature(°C)	T	25
Water-particle contact angle	θ	0
Barometric pressure (KPa)	P	101.325

3.6.1. Uniaxial Compression Testing (UCS). Uniaxial compression tests are simulated to assess the effects of moisture content on the granular assemblies' compressive strength. In the compressive test, particles are randomly generated in an L = 20 mm domain and H = 10 mm. The inter-particle friction coefficient is set to zero, and all the particles are consolidated under gravity until a static equilibrium state is obtained. Then the friction coefficient along with other parameters listed in **Table 1** are applied.
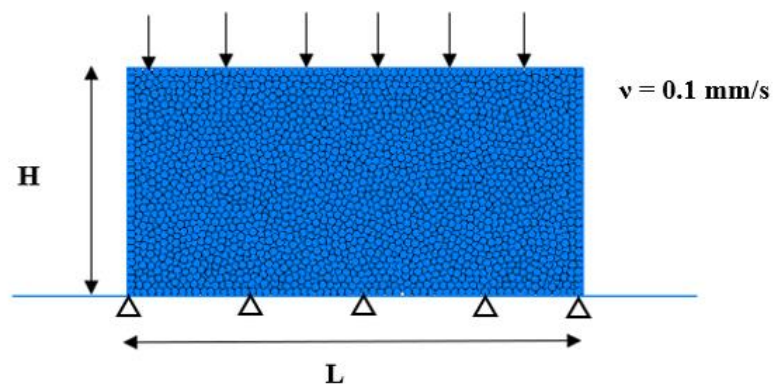

Figure 18. Uniaxial compressive test setup

The specimen is compressed by imparting a constant velocity of $\upsilon = 0.1$ mm/s (**Figure 18**) imparting from the top in the form of the wall, which applies the load while the bottom wall is fixed to restrict. The dimensions of the box and the model setup are demonstrated in **Figure 17**. The compressive force applied was shown in the form of stress, and the effect can be tracked in the form of a stress-stress curve. The values mentioned in **Table 3** are used for deriving the stress-strain curve from the simulation. The numerical simulation data is then compared with the experimental data. To understand each influence of the parametric studies is carried out.

3.7. Parametric Analysis

PFC^{2D} calculation program uses the micromechanics parameters to represent the particles of materials and the mechanical properties of their bonding. Before calculating the model's value, we must first assume several microscopic parameters for the model and compare the macroscopic mechanical properties and the results obtained in the laboratory. If the result is appropriate, we need to adjust the micromechanics parameters until the calculated results are almost the same as the experimental ones. Then these parameters can be applied to the actual model calculations. Therefore, the adjustment of microscopic mechanics parameters is fundamental [90].

The parametric study results are then discussed in Chapter 4, explaining the influence of each parameter on the model that affects the behavior of the material during the uniaxial compression.

Chapter 4

Results

4.1. Compression Test

To understand the hydrogel's mechanical properties and to use them as the input parameters in the numerical model, an uniaxial compression testing machine was operated to derive the stress-strain graph. The test was conducted under experimental conditions. Many tests have been completed, and intermediate values were selected as representative test results (**Figure 19**). The hydrogel's mechanical properties were calculated using the theoretical model, and the test results derived from the stress-strain graph are noted in **Table 4.1**.
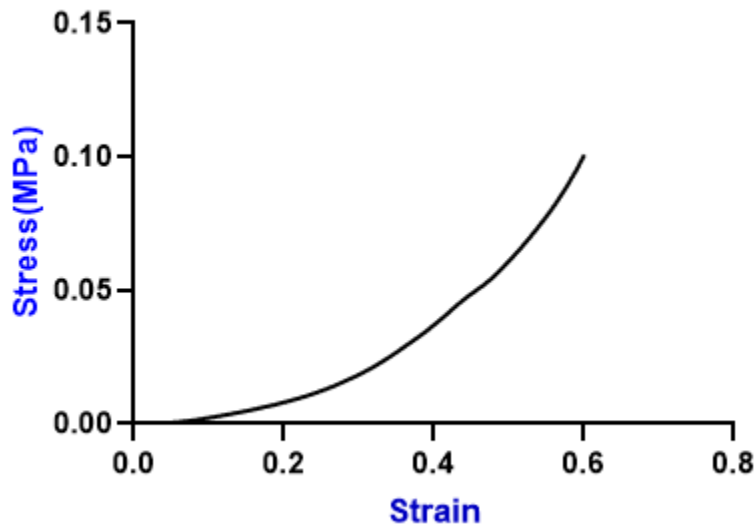

Figure 19. Stress-Strain under the confining pressure at 0.1 MPa

Table 3

Intact Hydrogel properties for analysis in PFC.

Test type	Parameter	Symbol	Value
Density test	Density (kg/m^3)	ρ	1140
UC test	UCS (MPa)	σ	0.1
	Elastic Modulus (MPa)	E	0.0039

4.2. Convergence Analysis

The Elastic Modulus was calculated for different particle sizes ranging from 100 µm to 1000 µm, and the Elastic modulus result ranged from 0.6 MPa to 6.3 MPa. **Figure 20** shows that the compressive strength of the model is directly proportional to the grain size opposing the Hall-Petch effect.

This point has a reasonable explanation, in DEM, the contact model plays a significant role in determining the material properties at each particle contact. The effect on the whole material at the contact location and the deformation is observed. The contact model used for modeling hydrogel is composed of linear elastic and liquid bridge volume. The primary parameter affecting the contact force model is COR, which restricts the particles' material flow and maintains a steady flow rate. The model's impact is shown using COR, which inputs the elasticity between the particles during the interaction while also accounting for minute friction. Due to this effect, the forces oppose the particle's motion and result in the particles in contact up to the level of external peak load on the combined material.

The particle or grain size affects the Elastic Modulus and has been affected by the contact model. There are many contact models applied at the interactions, and the

combined material consisting of the clump of particles is considered a single material. From the data extracted, 10 microns provide the best results based on the above discussion, which shows the precise value compared to the calibration data. Also, the convergence study was conducted at 1000 microns. It resulted in a high modulus of elasticity, and this is due to the particle being rigid and therefore does not follow any contact law. As a result, there is a high mechanical value; however, smaller particles have little influence on the model.

By taking the above statements and **Figure 20** into consideration, we concluded the particle size would be 100 µm for better analysis. But due to computational cost and speed of simulations, a particle size of 200 µm has been taken into consideration. The elastic modulus of both the particle ranges barely impacts the Modulus of Elasticity.
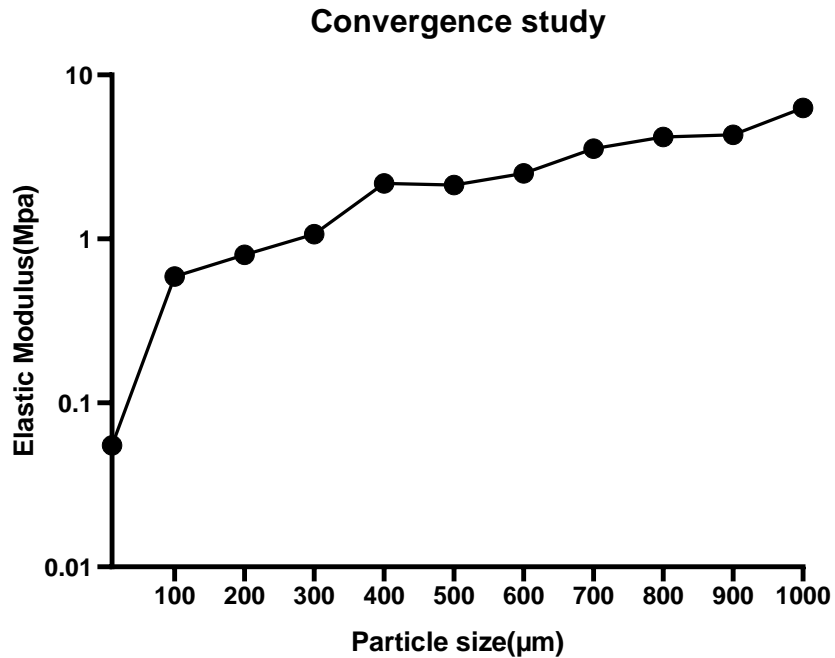

Figure 20. Convergence Analysis of Elastic Modulus at different particle sizes.

4.3. Parametric Study

4.3.1. Effect of Coefficient of Restitution (COR). Figure 21 the results from the compression test with different values of the coefficient of restitution (COR), ranging between 0 (Inelastic collision) to 1 (Elastic collision). Varying the COR in the range 0.2 – 1.0 leads to an increase in the stress (σ).
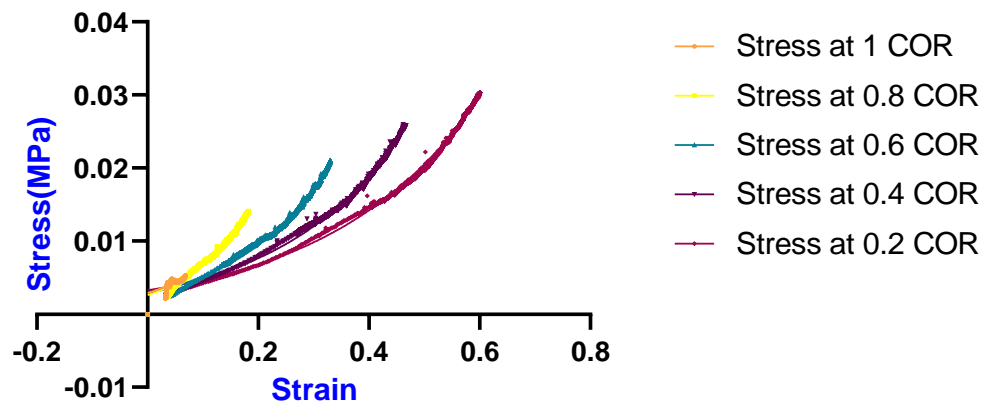

Figure 21. Stress-Strain curve with different Restitution Coefficients**.**

4.3.2. Effect of Static Friction Coefficient(μ). Figure 22 shows the static friction coefficient μ affects the stress-strain behavior of the granular materials. The stress increases with increasing μ at a similar strain level, which confirms the present results.
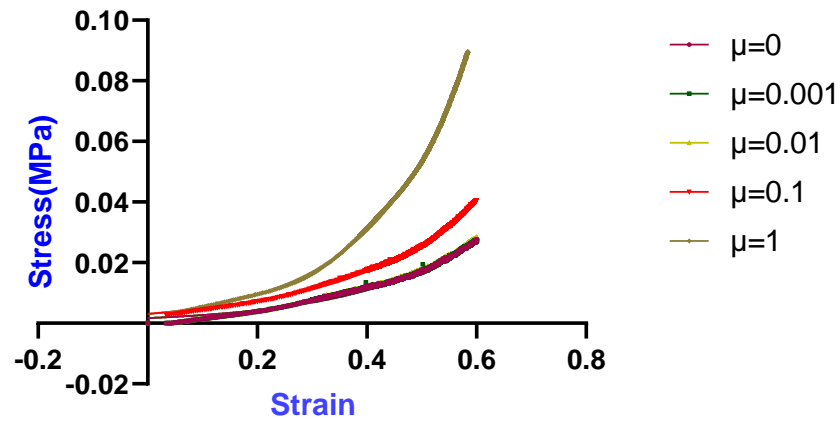
Figure 22. Stress-Strain curve with different Friction Coefficients.

The sample's peak strength increases with the particles' friction coefficient, representing a directly proportional relationship when the friction is small. The material exhibits the strain hardening characteristics. The larger the friction coefficient is, the more material will exhibit strain-softening characteristics. The material's residual strength also increases as the friction coefficient increases, but the change is small.

4.3.3. Effect of Stiffness Ratio (k_n / k_s). Under the conditions of a different stiffness ratio (normal stiffness / shear stiffness), respectively 0.0,0.5,1.5,2.5,3.5 and 4.5, the deviatoric stress-strain curves of samples are shown in **Figure 23**. As it can be seen, the stiffness ratio of the material has little effect on the stress-strain curve of the material, with little change to the peak strength and residual strength.
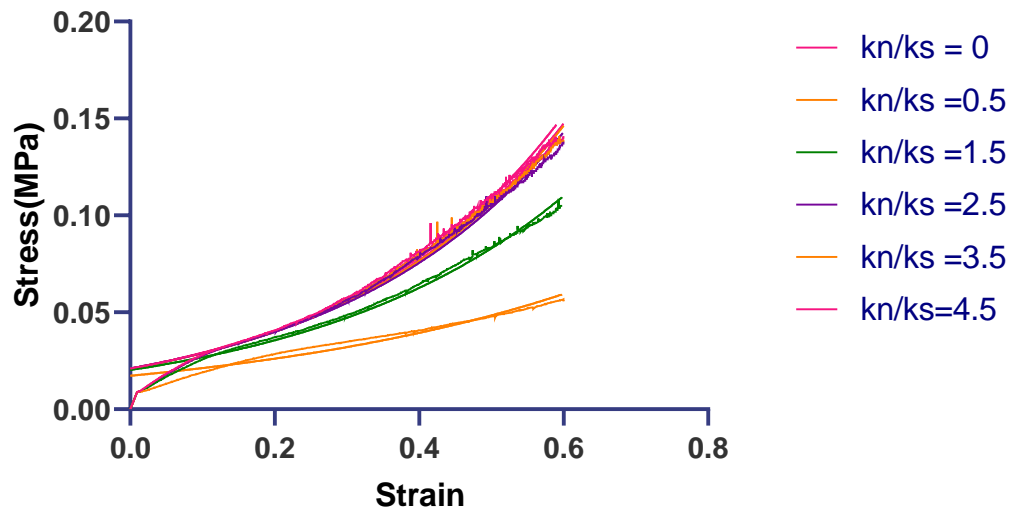
Figure 23. Stress-Strain curve at different Stiffness Ratio.

The above study was primarily conducted to understand the trends of various stress-strain curves upon the inputs of different values of the respective parameters. Three significant parameters were considered, which greatly influenced the model, to understand the model's changes. This analysis is fundamental, but it presents the impact of various parameters through this parametric study.

Chapter 5

Contact Force Analysis During Extrusion

5.1. Introduction

This study has been performed on the contact forces and subsequent force chain in a granular structure and observes the granular system's micro and mesoscopic properties in physical experiments. DEM has steadily become a useful tool to investigate the microscopic rules for granular systems. Besides, DEM has proven to replicate important characteristics of granular materials.

The idea of measuring the extrusion forces was proposed by Miri et al. (2019), where it states that the viscosity and nozzle speed affects the shear stress on the cells and period of extrusion. The forces that affect the shear rate are microscopic but can be represented macroscopically as a continuum, but the microscopic level cannot be measured. However, this gives a better idea of the forces' value by considering the total material as a clump of particles. The contact force model applies the behavior at the particle-interaction, which determines the interactional details. A few parameters are affecting the contact model that also impact the forces. The forces are updated based on the compression applied by the boundary condition of the wall.

As a part of Additive Manufacturing, we selected the extrusion-based deposition method to observe the micro-interactional forces at the particle contact during the materials' compression due to the pressure imparted by the piston.

5.2. Model Construction

The device's geometry is shown in **Figure 24** like a standard extrusion kind syringe only consisting of nozzle, needle, and the piston, developed with the help of walls, act as the boundary conditions. The material used is hydrogel in the form of particles. The properties of the hydrogel used in this modeling are derived from the calibration test analysis.
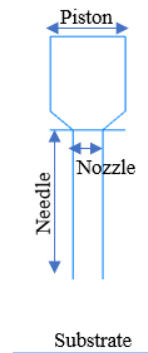

Figure 24. Geometry for the Extrusion printing.

The contact model of this extrusion process is a smart lobo linear model, and the particle generation and consolidation use the gravity accumulation method and perform out in the following steps:

1) Generation of initial particles: Through the ball generate command, several particles are formed in the range of x1, x2 along X-axis, and y1, y2 along Y-axis of the wall model with particle radius 10 µm. The gravitational acceleration of these particles is g = -9.81 m.s-2. To consolidate the particles by setting the

friction coefficient 0 and the particles' contact forces are represented in **Figure 24**.

2) Once the particles are positioned under gravity in the region, the piston is initiated, and a wall-like force is applied to push the material. The velocity of the wall is applied at a rate of 1mm/sec.

3) Generation of the calculating particle: For simulating the particles' influence, the particles' contact model is updated with different mechanical properties, as shown in **Table 4**. The particles are drawn downwards after deleting the wall at the nozzle during the extrusion. The force is calculated at the nozzle and needle at different sizes, respectively, using FISH of PFC^{2D} to compile loop statements in the process of extrusion while computing several time steps.
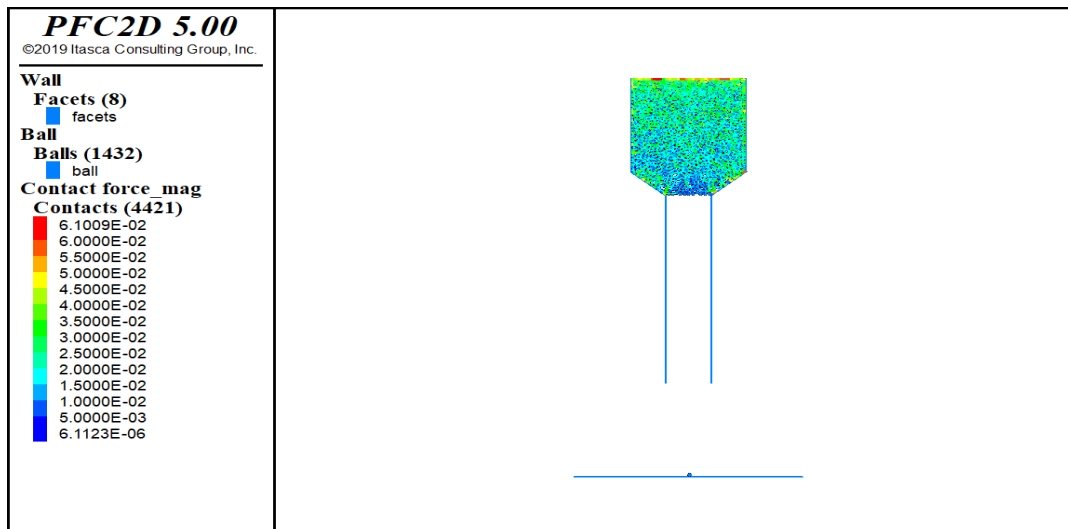

Figure 25. Contour plot representing contact forces between the particles during the consolidation under gravity acceleration

5.3. Force-Chain Component Ratio

The main parameter for characterizing the contact forces and the force chain at the microscale is calculated using the force-component ratio. The force chain component ratio quantitatively describes the force chain's total extension direction using the interactions between the contact force components in the-axis[91]. The calculation method is as follows:

$$\mu_c = \frac{\sum_{i=1}^{n} f_i^y - \sum_{i=1}^{n} f_i^x}{\sum_{i=1}^{n} f_i^y + \sum_{i=1}^{n} f_i^x} \qquad \text{(eq 5.1)}$$

where f_i^x represents the magnitude of the component of the contact force i on the x-axis, f_i^y represents the magnitude of the component of the contact force of contact i on the y-axis, n represents the total number of contacts, μ_c represents the force chain component ratio (when $\mu_c > 0$, the force chain is inclined to the vertical direction, that is, the y-axis direction; when $\mu_c < 0$, the force chain is inclined to the horizontal direction, that is, the x-axis direction). The more significant the difference between μ_c and 0 results in a more significant deflection of the force chain. In this paper, the force chain component ratio is calculated at various locations of the needle. The force chain is formed by the contact force created by all the contacts in the granular system.

The syringe model's extrusion process was carried with different nozzle diameters and needle lengths ranging from 200-500 µm and 0.25-1 mm, respectively. Our work mainly focuses on tracking the contact forces between the particles at different locations of the nozzle. A detailed contour plot and graphs were created to show the different contact forces at various points.

Table 4

Particle size and microscale parameters

Properties	Symbols	Values
Particle Density (kg/m^3)	ρ	1140
Particle radius (m)	r	0.0002
Elastic Modulus particle (MPa)	E	0.0039
Local damping ratio	β	0.5
Coefficient of restitution particle-particle	COR	0.1
Static friction coefficient particle-particle	μ	0.001
Normal to shear stiffness ratio	k_n / k_s	0.5
Cutoff-distance(nm)	z_0	0.5

5.4. Magnitudes of the Contact Force and its Distribution

The contact forces were derived at four different locations between the nozzle and where the material reaches the substrate at ten different positions, as shown in **Figure 26.** To understand how the force varies at the various positions, the nozzle and needle sizes were different. This is not possible during the experimental process and represented through PFC^{2D}.
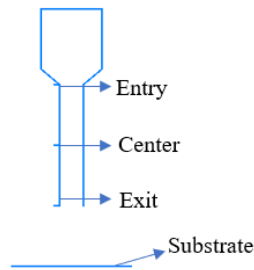

Figure 26. Contact forces are tracked at different locations, as represented.

The extrusion printing setup was constructed for the nozzle diameter of 200 microns. The particle size used was ten magnitudes less than the model's actual nozzle size, 20 microns. The model indicates the material is extruded from the nozzle through the needle and the needle length of 0.25 mm long. And this is repeated for various nozzle diameters of 300, 400, and 500 microns, and for each nozzle size, we used the needle lengths of 0.25mm, 0.5mm, and 1 mm. The forces at various locations along the needle distribution are recorded and plotted, as shown in **Figure 27**.
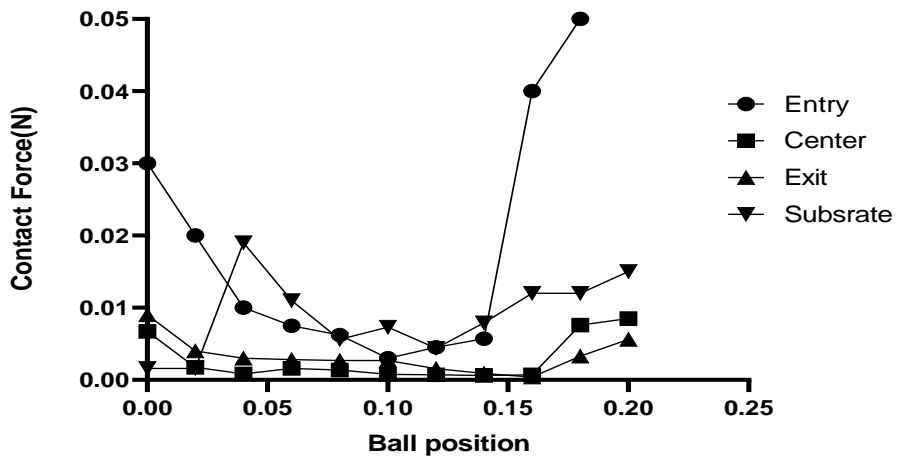

Figure 27. Contact forces vs. ball position graph at various locations of the model for nozzle size 200 µm and the needle length 0.25 mm.

The forces reach the maximum when the particle-wall interaction possesses high forces at both ends. An average force of 0.013 N follows the forces due to the gravity affected. At the center, the forces followed an equal force distribution of 0.0017 N, and the forces are reduced as the granular material flows downwards with a mean force of 0.0025 N at the

needle exit. Hence the material reaches substrate at a force rate of 0.0068 N due to the

wall's impact on the ball distribution.
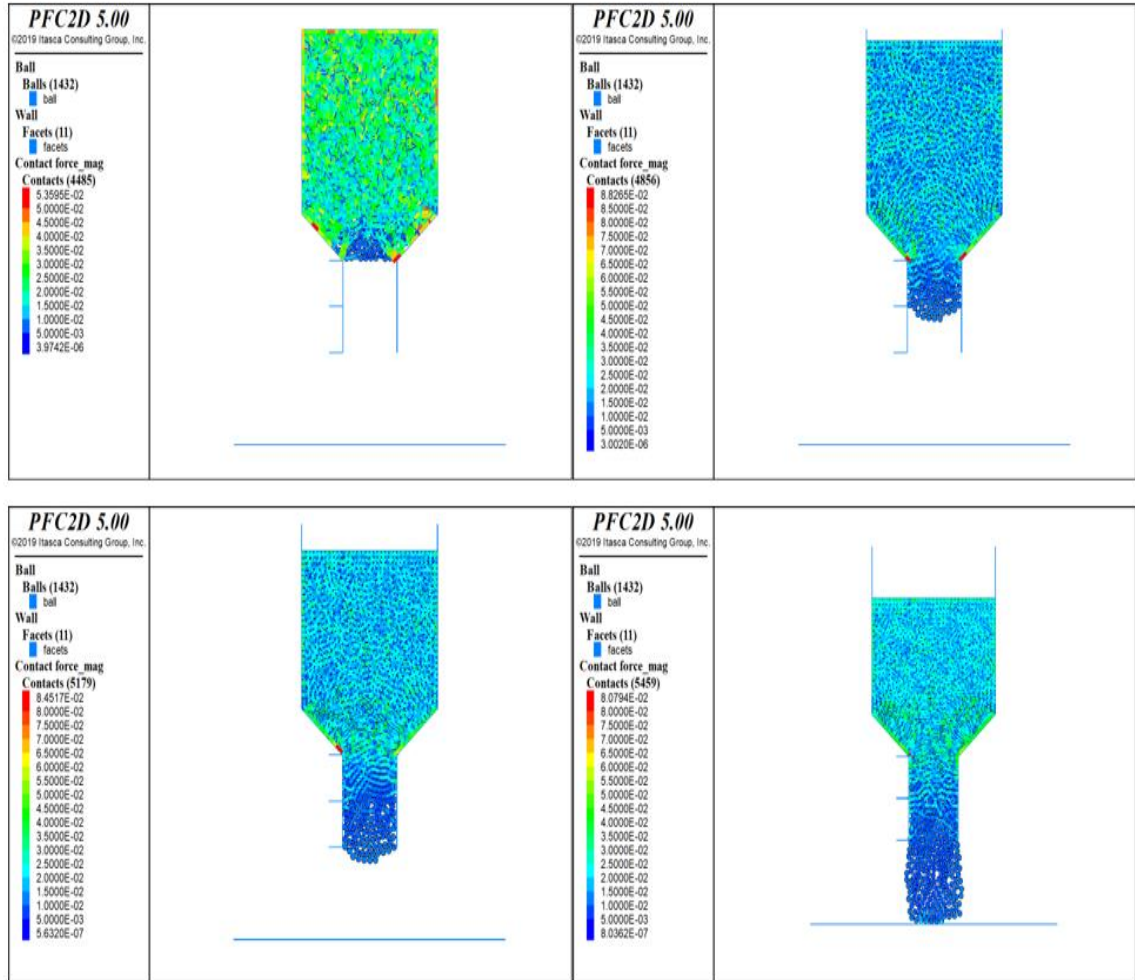
Figure 28. Contour plot for contact forces for nozzle size 200 µm and the needle length
0.25 mm.

The contour plot in **Figure 28** shows how the forces are changing due to the impact by the

piston pressure. The change in the color indicates the change in the forces along the needle.

During the update of the contact model, the forces are in equilibrium. At the entry, we can

observe the forces peak at the nozzle's corners, where red indicates the peak forces. As the

material gets depositing in the downward direction, we can observe the forces' change as the red color converted to green and blue, indicating the force fluctuations.

Table 5

Mean force distributions (N) along the needle were recorded for 200 μm.

Nozzle diameter (μm)	Needle length (mm)	Entry	Center	Exit	Substrate
200	0.25	0.01344	0.00169	0.00249	0.00688
200	0.5	0.01072	0.002241	0.00026	0.00264
200	1	0.00977	0.00147	0.00054	0.00167

The mean forces at different nozzle sizes and various needle size lengths recorded are tabulated in **Table 5**. And the percentage difference of the forces tracked is tabulated concerning primary mean force for 200 microns nozzle, and 0.25 mm needle size are tabulated in **Table 6**.

Table 6

Percentage difference (%) of mean forces along needle for nozzle size 200 μm

Nozzle diameter (μm)	Needle length (mm)	Entry	Center	Exit	Substrate
200	0.25	0	-87.4	-81.5	-48.8
200	0.5	-25.3	-83.3	-98.1	-80.3
200	1	-27.3	-89.1	-95.98	-87.6

In **Table 6**, we can observe that there is the minimum change in the forces at the nozzle for different lengths; however, we can see that the forces have their difference at a minimum

of 25 % decrease and a maximum of 98% decrease from the force at the nozzle from the nozzle entry.

Along with the nozzle size of 200 microns, the comparison data of forces for different nozzles were tabulated and listed according to their mean value at the specific location of the particles' clump during their flow inside the needle. The observation is very keen that the forces vary for multiple needle sizes and affect the deflection of the contact forces. The mean force distributions for various nozzle sizes are presented in tables that help to analyze how the forces act at various locations.

Table 7

Mean force distributions (N) along the needle were recorded for 300 μm.

Nozzle diameter (µm)	Needle length (mm)	Entry	Center	Exit	Substrate
300	0.25	0.01106	0.00209	0.00386	0.00176
300	0.5	0.00310	0.00223	0.00116	0.00539
300	1	0.00764	0.00114	0.00063	0.00129

The mean forces at different nozzle sizes and various needle size lengths recorded are tabulated in **Table 7**. And the percentage difference of the forces tracked is tabulated for the primary mean force for 300 microns nozzle, and 0.25 mm needle size is tabulated in **Table 8**.

Table 8

Percentage difference (%) of mean forces along needle for nozzle size 300 μm

Nozzle diameter (µm)	Needle length (mm)	Entry	Center	Exit	Substrate
300	0.25	0	-81.1	-65.1	-84.1
300	0.5	-71.9	-79.8	-89.5	-51.2
300	1	-30.9	-89.6	-94.3	-88.3

Table 8 shows a minimum charge in the forces at the nozzle for different lengths; however, we can see that the forces have their difference at a minimum of 30.9% and the maximum difference of 94.3% from the nozzle entry.

Table 9

Mean force distributions (N) along the needle recorded for 400 μm

Nozzle diameter (µm)	Needle length (mm)	Entry	Center	Exit	Substrate
400	0.25	0.00125	0.00041	0.00249	0.00140
400	0.5	0.00310	0.00200	0.00120	0.00406
400	1	0.00596	0.00111	0.00116	0.00189

The mean forces at different nozzle sizes and various needle size lengths recorded are tabulated in **Table 9**. And the percentage difference of the forces tracked is tabulated to primary mean force for 400 microns nozzle, and 0.25 mm needle size are tabulated in **Table 10**.

Table 10

Percentage difference (%) of mean forces along needle for nozzle size 400 μm

Nozzle diameter (μm)	Needle length (mm)	Entry	Center	Exit	Substrate
400	0.25	0	-67.2	99.2	11.9
400	0.5	147.8	60.0	-4.0	224.7
400	1	376.7	-11.1	-7.2	51.1

From **Table 10**, we can observe a minimum change in the forces at the nozzle for

different lengths. However, we can see that the forces have a percentage difference with

an increase of 376.7% maximum. The very minimum force difference is observed in the

percentage of 4% decrease from the nozzle entry.

Table 11

Mean force distributions (N) along the needle recorded for 500 μm

Nozzle diameter (μm)	Needle length (mm)	Entry	Center	Exit	Substrate
500	0.25	0.00830	0.0021	0.00197	0.00127
500	0.5	0.01037	0.00196	0.00134	0.0024
500	1	0.00323	0.00217	0.00117	0.00217

The mean forces for different nozzle sizes and various needle size lengths are tabulated in

Table 11. And the percentage difference of the forces tracked is tabulated for the primary

mean force for a 500 microns nozzle, and 0.25 mm needle size is tabulated in **Table 10**.

Table 12

Percentage difference (%) of mean forces along needle for nozzle size 500 μm

Nozzle diameter(μm)	Needle length(mm)	Entry	Center	Exit	Substrate
500	0.25	0	-74.6	-76.3	-84.6
500	0.5	24.9	-76.3	-83.8	-71.0
500	1	-61.1	-73.8	-85.9	-73.8

From **Table 12**, we can observe that there is a minimum deviation in the forces at the nozzle for different lengths. We can see that the forces have a percentage difference with an increase of 24.9% maximum, and the maximum force difference is observed in the decreased percentage of 85.9% from the nozzle entry. This shows that the forces are increased due to the impact of gravity on the model.

However, the results do not show much variance for the different sizes; however, this study is good practice for working with different gels by modeling them and using them for various applications in the future.

The above studies microscopic characteristics of the extrusion-pressed granular matter structure, but all these studies are in the preliminary phase of exploration; for quantitative study on contact force and force chain characteristics, there is no standardized framework.

Chapter 6

Conclusion and Future Work

6.1. Conclusion

The Elastic Modulus was measured for various particle sizes ranging from 100 μm to 1000 μm, and the Elastic Modulus result ranged from 0.6 MPa to 6.3 MPa. **Figure 20** shows that the model's compressive strength is directly proportional to the grain size instead of the Hall-Petch effect. Parametric Analysis showed valuable insights into the influence of the physical parameters on the model. Specific parameters that influence the model are stiffness ratio, COR, and friction coefficient.

Stiffness ratio influences the frequency of the contact force between the particle interaction at each particle-particle contact and is dependent on the elastic modulus of the material form that is introduced into the model, alters the stiffness ratio, and the stiffness ratio is inversely proportional to the Elastic modulus. The stress-strain Analysis has justified the properties. The COR follows the model by sustaining a collision between the particles with some form of model application. We know that the COR varies from 0 to 1, where 0 indicates the perfectly inelastic collision, and 1 indicates the perfect elastic collision. And the resulting graph presented the same evidence justifying the values.

The friction coefficient indicates the effect on the model by applying the opposite force in the applied force's direction where the value is about 0-1. Here, the greater the friction coefficient, the material will exhibit the softening properties of the pressure. The residual strength of the material will also increase as the friction coefficient increases. Out

of these parameters, the friction coefficient has shown a great deal of effect on the model developing maximum resistance forces in limiting the model's flow.

The values considered in the parametric Analysis were applied to the extrusion bioprinting application, where the forces are observed at the granular level during extrusion for various nozzle sizes and lengths of the needle. The power measured based on the plunger speed influences the substance inside the construction, and then we observed the pressures inside the hand at various points of the needle with the same needle lengths of 0.25 mm, 0.5 mm, and 1 mm.

Hence through this study, we worked to derive the properties of the granular gel-like liquid, which is Hydrogel where the DEM software was used for AM that helped in solving the analyzing the forces that affect the stresses of the Hydrogel during the extrusion, which impact the printing resolution and the shear rate that is affected by the pressure of the piston applied in the form of velocity.

6.2. Future Work

During this research, a lot of new ideas have been raised that might lead to continued work. There are few things which can be focused on for the continuation of this project. The convergence study found the correlation between the particle size and the elastic modulus. To further proceed the work the comparison between the particle size and the Van der Waals forces during model formation. We observed the effect of the capillary forces on the particle size where the model uses lower capillary forces.

During the parametric study, the influence of the stiffness ratio, COR, and friction on the model have been found. However, observation is needed for the other parameters such as Van der Waals force and water content affecting the capillary forces through liquid bridge volume. The parametric study conducted was based on uniaxial compression on the model however the analysis is conducted based on the repose test and the spreading test.

For contact force analysis, we used an extrusion process for observing the forces at various locations of different nozzle and needle sizes. This study can be used to in further studies involving different mechanisms of extrusion for different plunger speeds and observing the influence of a plunger on particles and forces. This helps demonstrate the effect of bioink velocity on the stresses inside the bioink material. Also, the forces were observed for the spreading test and repose test with the same material properties. And I strongly recommend that various fluid-gel like materials is modeled using DEM method. This method gives an opportunity to observe the forces for different materials at a microstructure level.

References

[1] R. D. Murphy, S. Kimmins, A. J. Hibbitts, and A. Heise, "3D-extrusion printing of stable constructs composed of photoresponsive polypeptide hydrogels," *Polym. Chem.*, vol. 10, no. 34, pp. 4675–4682, Sep. 2019, doi: 10.1039/c9py00796b.

[2] C. E. Berrimi and A. Chaparala, "A STUDY ON THE SURFACE TOPOGRAPHY AND DIMENSIONAL ACCURACY OF FUSED DEPOSITION MODELING: THE EFFECTS OF SURFACE ORIENTATION AND DIFFERENT PRINT SETTINGS." 2017.

[3] L. Overmeyer, A. Neumeister, and R. Kling, "Direct precision manufacturing of three-dimensional components using organically modified ceramics," *CIRP Ann.*, vol. 60, no. 1, pp. 267–270, 2011.

[4] J. Stampfl *et al.*, "Photopolymers with tunable mechanical properties processed by laser-based high-resolution stereolithography," *J. Micromechanics Microengineering*, vol. 18, no. 12, p. 125014, 2008.

[5] G. N. Levy, R. Schindel, and J.-P. Kruth, "Rapid manufacturing and rapid tooling with layer manufacturing (LM) technologies, state of the art and future perspectives," *CIRP Ann.*, vol. 52, no. 2, pp. 589–609, 2003.

[6] V. S. D. Voet *et al.*, "Biobased acrylate photocurable resin formulation for stereolithography 3D printing," *ACS omega*, vol. 3, no. 2, pp. 1403–1408, 2018.

[7] B. Cotur and H. K. Sezer, "Current 3 Dimensional Printing Technologies Used in Scaffold Design in Tissue Engineering," vol. 5, p. 548, Jul. 2017.

[8] H. M. Aydin, A. J. El Haj, E. Pişkin, and Y. Yang, "Improving pore interconnectivity in polymeric scaffolds for tissue engineering," *J. Tissue Eng. Regen. Med.*, vol. 3, no. 6, pp. 470–476, 2009.

[9] S. Amini-Nik, Y. Yousuf, and M. G. Jeschke, "Scar management in burn injuries using drug delivery and molecular signaling: current treatments and future directions," *Adv. Drug Deliv. Rev.*, vol. 123, pp. 135–154, 2018.

[10] L. Koch *et al.*, "Skin tissue generation by laser cell printing," *Biotechnol. Bioeng.*, vol. 109, no. 7, pp. 1855–1863, 2012.

[11] G. Cittadella Vigodarzere and S. Mantero, "Skeletal muscle tissue engineering: strategies for volumetric constructs," *Front. Physiol.*, vol. 5, p. 362, 2014.

[12] Y.-C. Huang, R. G. Dennis, L. Larkin, and K. Baar, "Rapid formation of functional muscle in vitro using fibrin gels," *J. Appl. Physiol.*, vol. 98, no. 2, pp. 706–713, 2005.

[13] W. Yan *et al.*, "Tissue engineering of skeletal muscle," *Tissue Eng.*, vol. 13, no. 11, pp. 2781–2790, 2007.

[14] S. Laternser, H. Keller, O. Leupin, M. Rausch, U. Graf-Hausner, and M. Rimann, "A novel microplate 3D bioprinting platform for the engineering of muscle and tendon tissues," *SLAS Technol. Transl. Life Sci. Innov.*, vol. 23, no. 6, pp. 599–613, 2018.

[15] N. E. Yin-kwee, *Cardiac perfusion and pumping engineering*, vol. 1. World Scientific, 2007.

[16] V. G. Fast, "Darrow BJ, Saffitz JE, and Kleber AG," *Anisotropic Act. spread Hear. cell monolayers Assess. by high-resolution Opt. mapping. Role tissue discontinuities. Circ Res*, vol. 79, pp. 115–127, 1996.

[17] H. Bien, L. Yin, and E. Entcheva, "Cardiac cell networks on elastic microgrooved scaffolds," *IEEE Eng. Med. Biol. Mag.*, vol. 22, no. 5, pp. 108–112, 2003.

[18] Y. S. Zhang *et al.*, "Bioprinting 3D microfibrous scaffolds for engineering endothelialized myocardium and heart-on-a-chip," *Biomaterials*, vol. 110, pp. 45–59, 2016.

[19] S. Boularaoui, G. Al Hussein, K. A. Khan, N. Christoforou, and C. Stefanini, "An overview of extrusion-based bioprinting with a focus on induced shear stress and its effect on cell viability," *Bioprinting*, p. e00093, 2020.

[20] S. V Murphy and A. Atala, "3D bioprinting of tissues and organs," *Nat. Biotechnol.*, vol. 32, no. 8, pp. 773–785, 2014.

[21] D. Huh, G. A. Hamilton, and D. E. Ingber, "From 3D cell culture to organs-on-chips," *Trends Cell Biol.*, vol. 21, no. 12, pp. 745–754, 2011.

[22] A. K. Miri *et al.*, "Effective bioprinting resolution in tissue model fabrication," *Lab Chip*, 2019, doi: 10.1039/C8LC01037D.

[23] I. T. Ozbolat and M. Hospodiuk, "Current advances and future perspectives in extrusion-based bioprinting," *Biomaterials*, vol. 76, pp. 321–343, 2016.

[24] B. Derby, "Printing and prototyping of tissues and scaffolds," *Science (80-.).*, vol. 338, no. 6109, pp. 921–926, 2012.

[25] K. Hölzl, S. Lin, L. Tytgat, S. Van Vlierberghe, L. Gu, and A. Ovsianikov, "Bioink properties before, during and after 3D bioprinting," *Biofabrication*, vol. 8, no. 3, p. 32002, 2016.

[26] T. Jungst, W. Smolan, K. Schacht, T. Scheibel, and J. Groll, "Strategies and molecular design criteria for 3D printable hydrogels," *Chem. Rev.*, vol. 116, no. 3, pp. 1496–1539, 2016.

[27] C. K. Chua and W. Y. Yeong, "Materials for bioprinting," *Bioprinting Princ. Appl. Singapore World Sci. Publ. Co. Pte. Ltd*, pp. 117–164, 2014.

[28] J. Cheng *et al.*, "Rheological properties of cell-hydrogel composites extruding through small-diameter tips," *J. Manuf. Sci. Eng.*, vol. 130, no. 2, 2008.

[29] A. N. Boto, P. Kok, D. S. Abrams, S. L. Braunstein, C. P. Williams, and J. P. Dowling, "Quantum interferometric optical lithography: exploiting entanglement to beat the diffraction limit," *Phys. Rev. Lett.*, vol. 85, no. 13, p. 2733, 2000.

[30] H. Lipson, F. C. Moon, J. Hai, and C. Paventi, "3-D printing the history of mechanisms," 2005.

[31] J.-P. Fouassier and J. Lalevée, *Photoinitiators for polymer synthesis: scope, reactivity, and efficiency*. John Wiley & Sons, 2012.

[32] Formlabs.Inc, *Guide to Stereolithography (SLA) 3D Printing in 2020*. 2020.

[33] D. A. Foyt, M. D. A. Norman, T. T. L. Yu, and E. Gentleman, "Exploiting advanced hydrogel technologies to address key challenges in regenerative medicine," *Adv. Healthc. Mater.*, vol. 7, no. 8, p. 1700939, 2018.

[34] E. M. Ahmed, "Hydrogel: Preparation, characterization, and applications: A review," *J. Adv. Res.*, vol. 6, no. 2, pp. 105–121, 2015.

[35] P. E. Grimshaw, "Electrical control of solute transport across polyelectrolyte membranes." 1989.

[36] F. Ganji, F. S. Vasheghani, and F. E. VASHEGHANI, "Theoretical description of hydrogel swelling: a review," 2010.

[37] L. Ma *et al.*, "Collagen/chitosan porous scaffolds with improved biostability for skin tissue engineering," *Biomaterials*, vol. 24, no. 26, pp. 4833–4841, 2003.

[38] S. S. Silva, J. F. Mano, and R. L. Reis, "Potential applications of natural origin polymer-based systems in soft tissue regeneration," *Crit. Rev. Biotechnol.*, vol. 30, no. 3, pp. 200–221, 2010.

[39] L. Francis *et al.*, "Development of a novel hybrid bioactive hydrogel for future clinical applications," *J. Biomater. Appl.*, vol. 33, no. 3, pp. 447–465, 2018.

[40] K. Liu and T. C. Ovaert, "Poro-viscoelastic constitutive modeling of unconfined creep of hydrogels using finite element analysis with integrated optimization method," *J. Mech. Behav. Biomed. Mater.*, vol. 4, no. 3, pp. 440–450, 2011, doi: 10.1016/j.jmbbm.2010.12.005.

[41] J. H. Ferziger, M. Perić, and R. L. Street, *Computational methods for fluid dynamics*, vol. 3. Springer, 2002.

[42] A. D. Polyanin, W. E. Schiesser, and A. I. Zhurov, "Partial differential equation," *Scholarpedia*, vol. 3, no. 10, p. 4605, 2008.

[43] D. Caccavo, S. Cascone, G. Lamberti, and A. A. Barba, "Hydrogels: experimental characterization and mathematical modelling of their mechanical and diffusive behaviour," *Chem. Soc. Rev.*, vol. 47, no. 7, pp. 2357–2373, 2018.

[44] A. Ismail-Zadeh and P. Tackley, *Computational methods for geodynamics*. Cambridge University Press, 2010.

[45] and D. S. Stephen Edwards, Brian Dorn, "Problem Solving and Algorithms," *Objects First*, 2012. http://sofia.cs.vt.edu/cs1114-ebooklet/chapter4.html.

[46] D. L. Logan, *A first course in the finite element method*. Cengage Learning, 2011.

[47] F. Yang, C. Guo, M. Zhang, B. Bhandari, and Y. Liu, "LWT - Food Science and Technology Improving 3D printing process of lemon juice gel based on fl uid fl ow numerical simulation," vol. 102, no. November 2018, pp. 89–99, 2019.

[48] "Cundall&Strack(1979).pdf." .

[49] H. G. Matuttis, S. Luding, and H. J. Herrmann, "Discrete element simulations of dense packings and heaps made of spherical and non-spherical particles," pp. 278–292, 2000.

[50] A. Anand, J. S. Curtis, C. R. Wassgren, B. C. Hancock, and W. R. Ketterhagen, "Predicting discharge dynamics from a rectangular hopper using the discrete element method (DEM)," vol. 63, 2008, doi: 10.1016/j.ces.2008.08.015.

[51] D. Potyondy, "ITASCA Consulting Group Memorandum," no. ICG7766-L, 2019, [Online]. Available: https://www.itasca-africa.co.za/software/material-modeling-support-download-files.

[52] P. A. Cundall, "A computer model for simulating progressive, large-scale movement in blocky rock system," 1971.

[53] P. A. Cundall, "A computer model for rock mass behavior using interactive graphics for the input and output of geometrical data," *A Rep. Prep. under Contract Number DACW 45-74-C-006, Missouri River Div.*, 1974.

[54] P. A. Cundall and O. D. L. Strack, "A discrete numerical model for granular assemblies," *geotechnique*, vol. 29, no. 1, pp. 47–65, 1979.

[55] P. A. Cundall and R. D. Hart, "Numerical modelling of discontinua," *Eng. Comput.*, 1992.

[56] D. O. Potyondy and P. A. Cundall, "A bonded-particle model for rock," *Int. J. Rock Mech. Min. Sci.*, vol. 41, no. 8 SPEC.ISS., pp. 1329–1364, 2004, doi: 10.1016/j.ijrmms.2004.09.011.

[57] Y. Ma, T. M. Evans, N. Philips, and N. Cunningham, "Numerical simulation of the effect of fine fraction on the flowability of powders in additive manufacturing," *Powder Technol.*, vol. 360, pp. 608–621, 2020.

[58] T. Kawaguchi, "Numerical simulation of fluidized bed using the distinct element method (the case of spouting bed)," *Trans. JSME, B*, vol. 58, pp. 2119–2124, 1992.

[59] P. W. Cleary, "DEM prediction of industrial and geophysical particle flows," *Particuology*, vol. 8, no. 2, pp. 106–118, 2010.

[60] Y. Chen, Y. Zhao, H. Gao, and J. Zheng, "Liquid bridge force between two unequal-sized spheres or a sphere and a plane," *Particuology*, vol. 9, no. 4, pp. 374–380, 2011.

[61] C. D. Willett, M. J. Adams, S. A. Johnson, and J. P. K. Seville, "Capillary bridges between two spherical bodies," *Langmuir*, vol. 16, no. 24, pp. 9396–9405, 2000.

[62] F. Zhou and Q. Ma, "Exact solution for capillary interactions between two particles with fixed liquid volume," *Appl. Math. Mech.*, vol. 37, no. 12, pp. 1597–1606, 2016.

[63] M. A. Erle, D. C. Dyson, and N. R. Morrow, "Liquid bridges between cylinders, in a torus, and between spheres," *AIChE J.*, vol. 17, no. 1, pp. 115–121, 1971.

[64] G. Lian, C. Thornton, and M. J. Adams, "A theoretical study of the liquid bridge forces between two rigid spherical bodies," *J. Colloid Interface Sci.*, vol. 161, no. 1, pp. 138–147, 1993.

[65] T. Mikami, H. Kamiya, and M. Horio, "Numerical simulation of cohesive powder behavior in a fluidized bed," *Chem. Eng. Sci.*, vol. 53, no. 10, pp. 1927–1940, 1998.

[66] Y. I. Rabinovich, M. S. Esayanur, and B. M. Moudgil, "Capillary forces between two spheres with a fixed volume liquid bridge: theory and experiment," *Langmuir*, vol. 21, no. 24, pp. 10992–10997, 2005.

[67] F. R. E. De Bisschop and W. J. L. Rigole, "A physical model for liquid capillary bridges between adsorptive solid spheres: the nodoid of plateau," *J. Colloid Interface Sci.*, vol. 88, no. 1, pp. 117–128, 1982.

[68] A. Gladkyy and R. Schwarze, "Comparison of different capillary bridge models for application in the discrete element method," *Granul. Matter*, vol. 16, no. 6, pp. 911–920, 2014.

[69] V. Richefeu, M. S. El Youssoufi, R. Peyroux, and F. Radjai, "A model of capillary cohesion for numerical simulations of 3D polydisperse granular media," *Int. J. Numer. Anal. Methods Geomech.*, vol. 32, no. 11, pp. 1365–1383, 2008.

[70] F. Soulie, F. Cherblanc, M. S. El Youssoufi, and C. Saix, "Influence of liquid bridges on the mechanical behaviour of polydisperse granular materials," *Int. J. Numer. Anal. methods Geomech.*, vol. 30, no. 3, pp. 213–228, 2006.

[71] G. Lian, C. Thornton, and M. J. Adams, "Discrete particle simulation of agglomerate impact coalescence," *Chem. Eng. Sci.*, vol. 53, no. 19, pp. 3381–3391, 1998.

[72] M. G. Lawrence, "The relationship between relative humidity and the dewpoint temperature in moist air: A simple conversion and applications," *Bull. Am. Meteorol. Soc.*, vol. 86, no. 2, pp. 225–234, 2005.

[73] O. A. Alduchov and R. E. Eskridge, "Improved Magnus form approximation of saturation vapor pressure," *J. Appl. Meteorol.*, vol. 35, no. 4, pp. 601–609, 1996.

[74] É. Clapeyron, "Mémoire sur la puissance motrice de la chaleur," *J. l'École Polytech.*, vol. 14, pp. 153–190, 1834.

[75] J. Olmsted and G. M. Williams, "Chemistry, the molecular science, mosby, st," *Louis, MO*, 1994.

[76] P. Hobza, R. Zahradník, and M. STULIKOVA, "Intermolecular complexes: the role of van der Waals systems in physical chemistry and in the biodisciplines," *Stud. Phys. Theor. Chem.*, vol. 52, pp. 1–307, 1988.

[77] Q. Li, V. Rudolph, B. Weigl, and A. Earl, "Interparticle van der Waals force in powder flowability and compactibility," *Int. J. Pharm.*, vol. 280, no. 1–2, pp. 77–93, 2004.

[78] L. Yang, J. Hu, and K. Bai, "Capillary and van der Waals force between microparticles with different sizes in humid air," *J. Adhes. Sci. Technol.*, vol. 30, no. 5, pp. 566–578, 2016.

[79] T. Stifter, O. Marti, and B. Bhushan, "Theoretical investigation of the distance dependence of capillary and van der Waals forces in scanning force microscopy," *Phys. Rev. B*, vol. 62, no. 20, p. 13667, 2000.

[80] H. C. Hamaker, "The London—van der Waals attraction between spherical particles," *physica*, vol. 4, no. 10, pp. 1058–1072, 1937.

[81] L. Aarons and S. Sundaresan, "Shear flow of assemblies of cohesive and non-cohesive granular materials," *Powder Technol.*, vol. 169, no. 1, pp. 10–21, 2006.

[82] H. Abbasfard, G. Evans, and R. Moreno-Atanasio, "Effect of van der Waals force cut-off distance on adhesive collision parameters in DEM simulation," *Powder Technol.*, vol. 299, pp. 9–18, 2016.

[83] E. J. R. Parteli and T. Pöschel, "Particle-based simulation of powder application in additive manufacturing," *Powder Technol.*, vol. 288, pp. 96–102, 2016.

[84] A. Castellanos, "The relationship between attractive interparticle forces and bulk behaviour in dry and uncharged fine powders," *Adv. Phys.*, vol. 54, no. 4, pp. 263–376, 2005.

[85] J.-F. Jerier, V. Richefeu, D. Imbault, and F.-V. Donzé, "Packing spherical discrete elements for large scale simulations," *Comput. Methods Appl. Mech. Eng.*, vol. 199, no. 25–28, pp. 1668–1676, 2010.

[86] T. C. Hales, "An overview of the Kepler conjecture," *arXiv Prepr. math/9811071*, 1998.

[87] K. Pal, A. K. Banthia, and D. K. Majumdar, "Polyvinyl alcohol—gelatin patches of salicylic acid: preparation, characterization and drug release studies," *J. Biomater. Appl.*, vol. 21, no. 1, pp. 75–91, 2006.

[88] J.-W. Jiang, J.-S. Wang, and B. Li, "Young's modulus of graphene: a molecular dynamics study," *Phys. Rev. B*, vol. 80, no. 11, p. 113405, 2009.

[89] H. Atapour and A. Mortazavi, "The influence of mean grain size on unconfined compressive strength of weakly consolidated reservoir sandstones," *J. Pet. Sci. Eng.*, vol. 171, pp. 63–70, 2018.

[90] Z. Yuan, "Microscopic Mechanics of Soil Failure and PFC Numerical Simulation [D]," *Tongji Univ.*, 2006.

[91] W. Zhang, J. Zhou, S. W. Yu, X. Zhang, and K. Liu, "Quantitative investigation on force chains of metal powder in high velocity compaction by using discrete element method," *J. Mech. Eng.*, vol. 54, no. 10, pp. 85–92, 2018.

[92] A. K. Miri, A. Khalilpour, B. Cecen, S. Maharjan, S. R. Shin, and A. Khademhosseini, "Multiscale bioprinting of vascularized models," *Biomaterials*, vol. 198, pp. 204–216, 2019.

[93] A. K. Miri *et al.*, "Microfluidics-enabled multimaterial maskless stereolithographic bioprinting," *Adv. Mater.*, vol. 30, no. 27, p. 1800242, 2018.

[94] R. Schwartz, M. Malpica, G. L. Thompson, and A. K. Miri, "Cell encapsulation in gelatin bioink impairs 3D bioprinting resolution," *J. Mech. Behav. Biomed. Mater.*, vol. 103, p. 103524, 2020.

Appendix A

Supplementary Figures

1) **At nozzle size 200 µm and the needle length 0.5 mm**
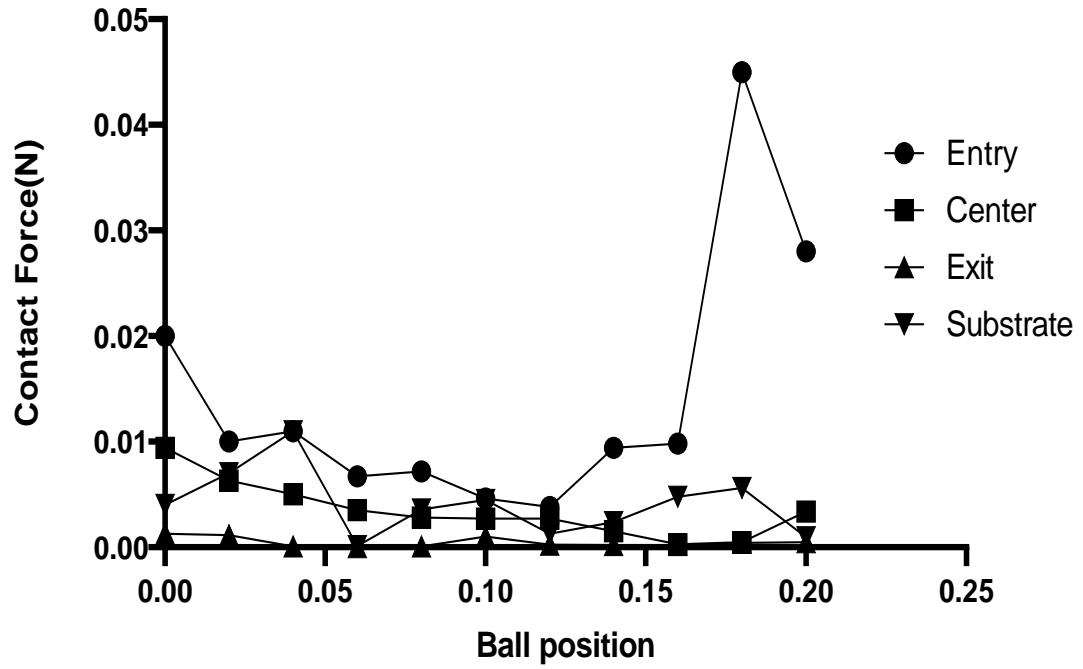
Figure A1. Contact forces vs ball position graph at various locations of the model for

nozzle size 200 µm and the needle length 0.5 mm.
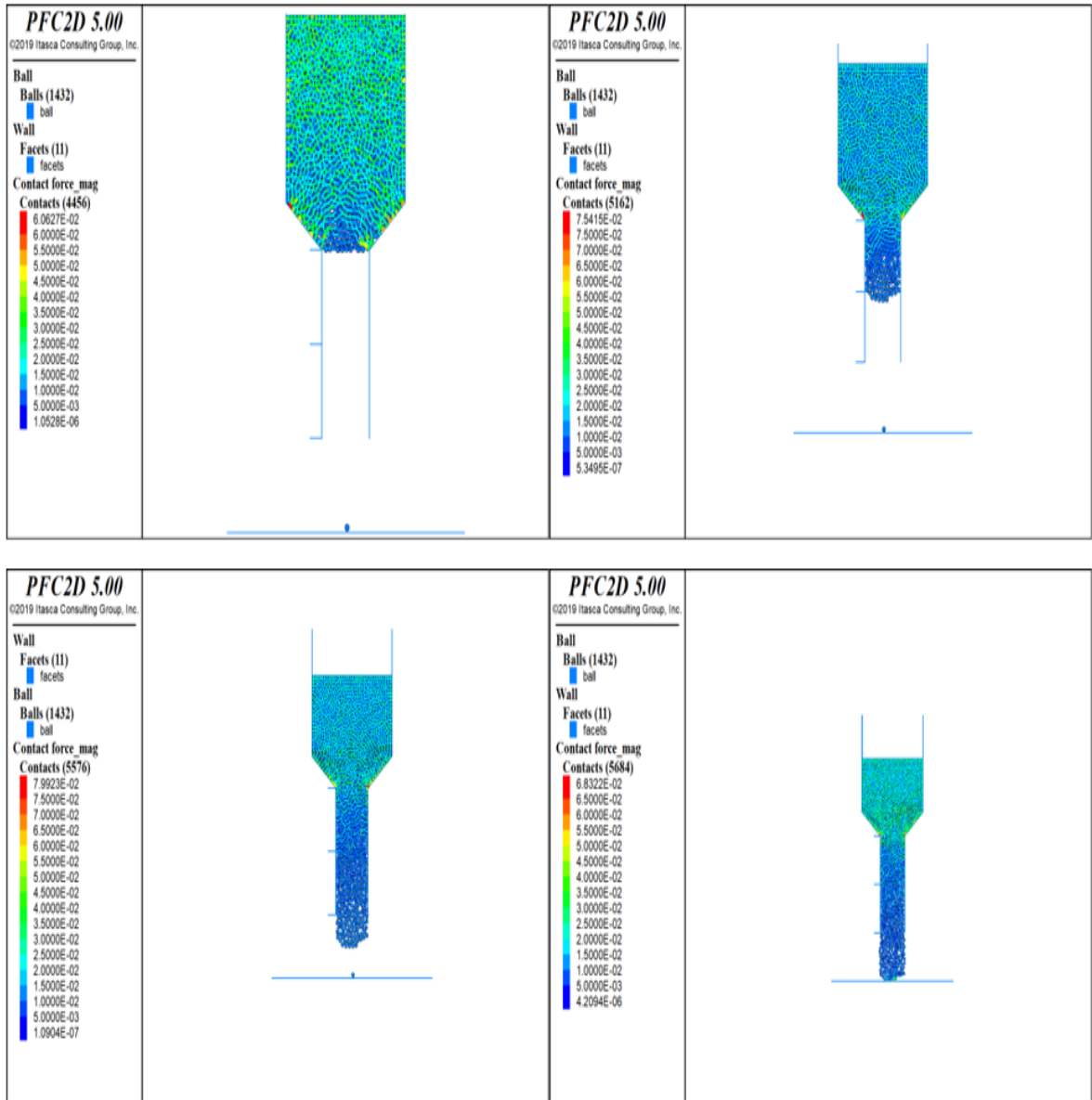
Figure A2. Contour plot for contact forces between for nozzle size 200 μm and the needle length 0.25 mm.

**2) At nozzle size 200 μm and the needle length 1 mm**
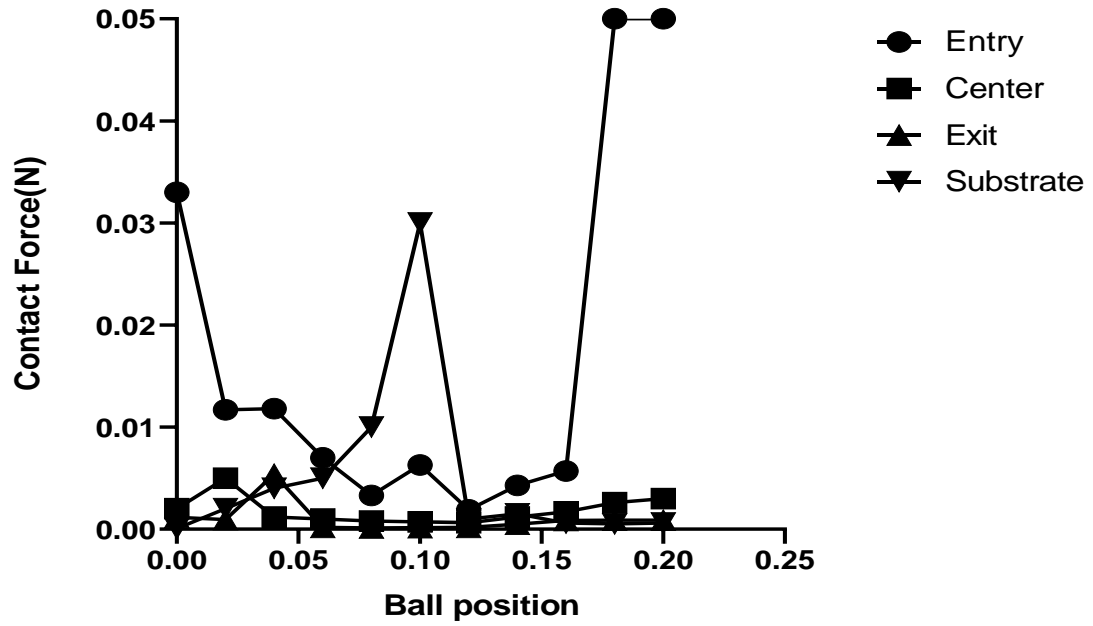
Figure A3. Contact forces vs ball position graph at various locations of the model for nozzle size 200 μm and the needle length 1 mm.
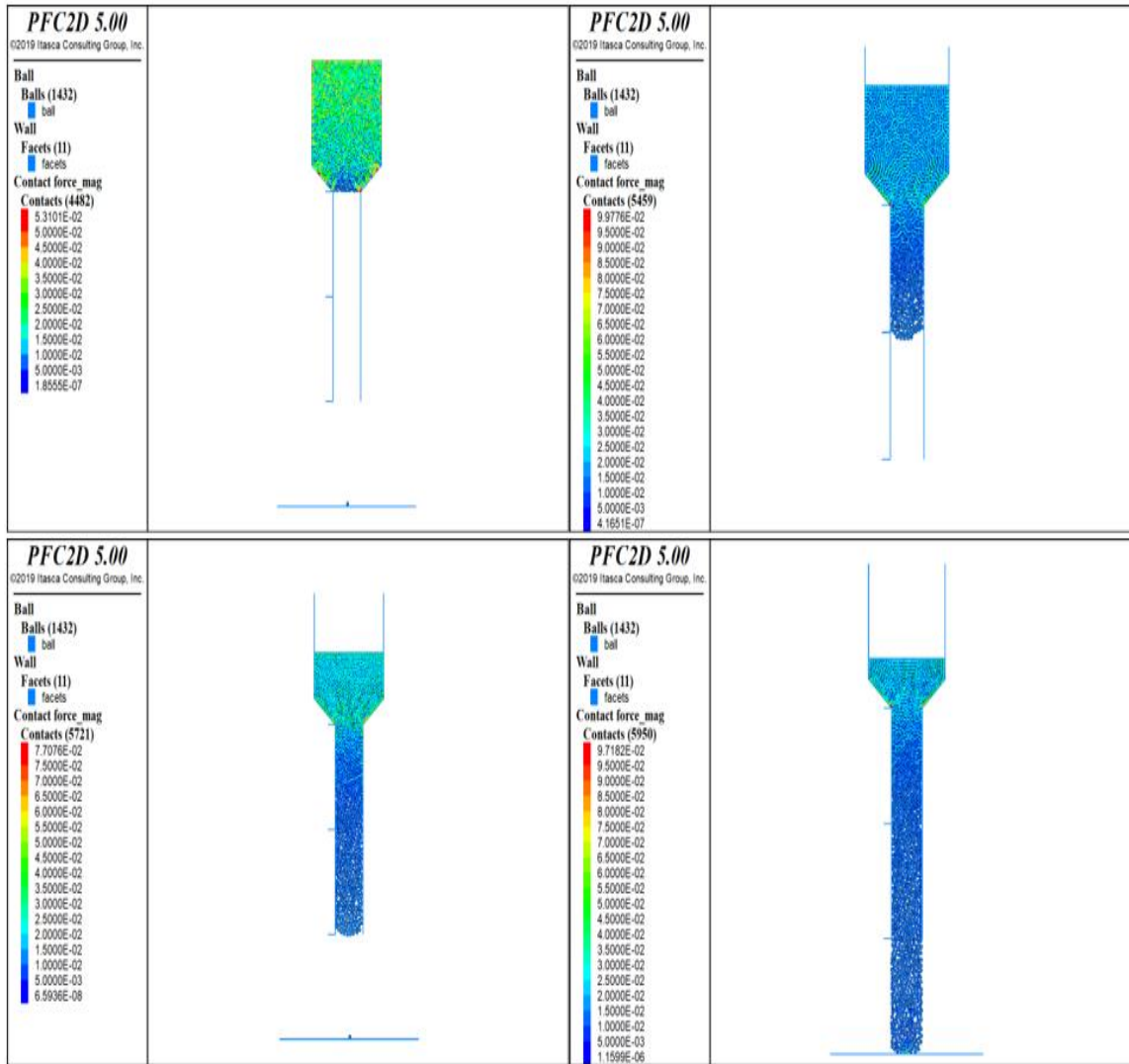
*Figure A4*. Contour plot for contact forces between for nozzle size 200 µm and the needle length 1 mm.

3) At nozzle size 300 µm and the needle length 0.25 mm
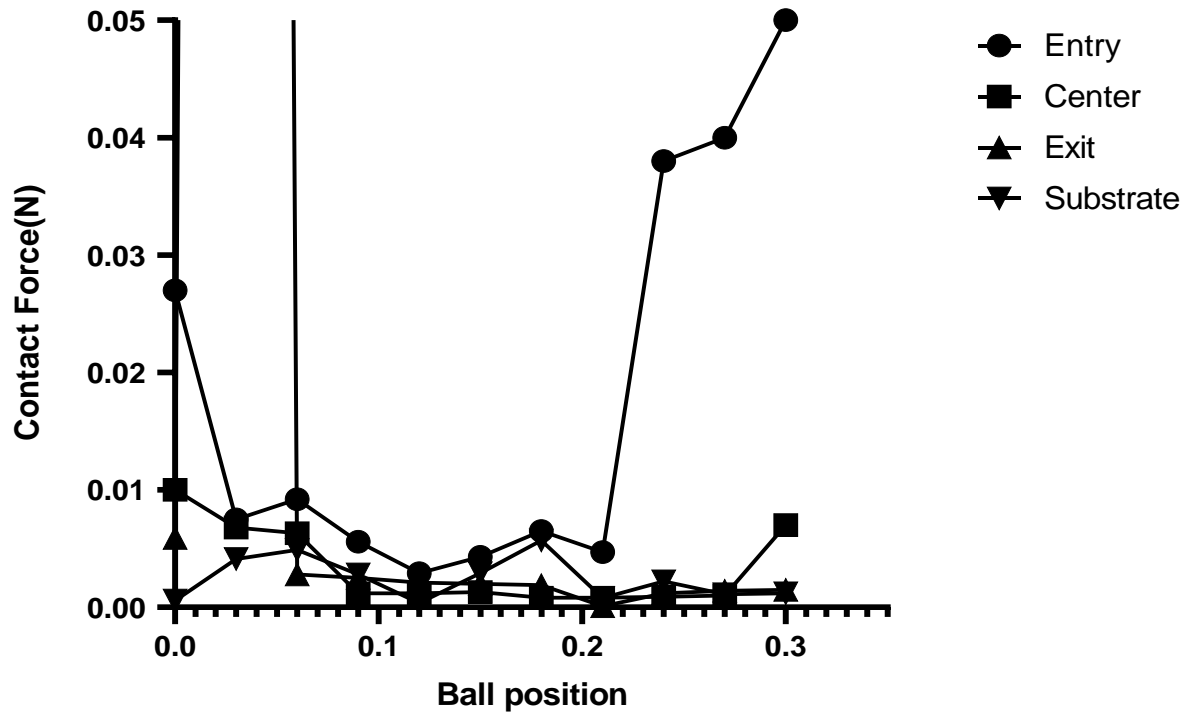
*Figure A5*. Contact forces vs ball position graph at various locations of the model for nozzle size 300 µm and the needle length 0.25 mm.
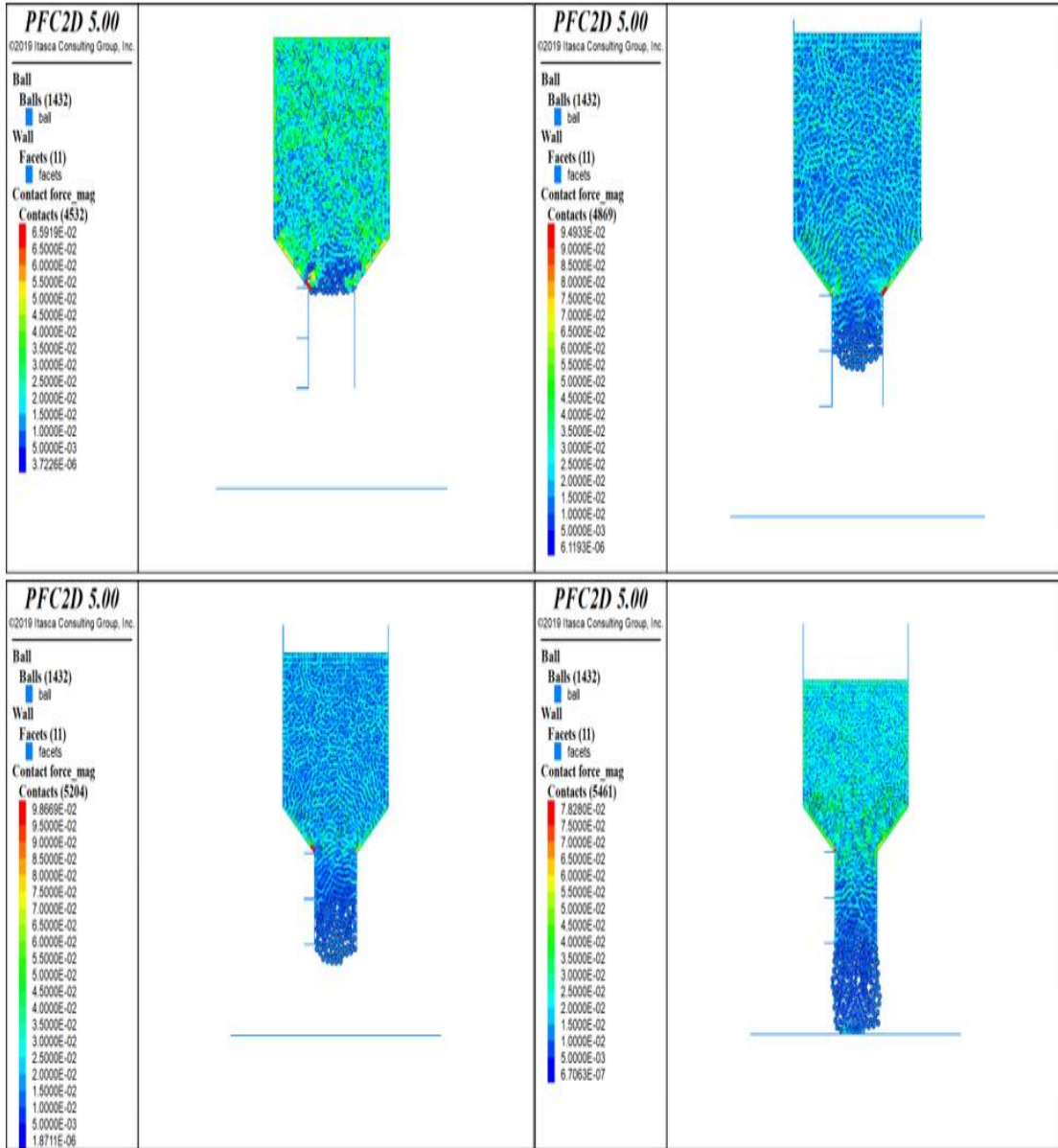
Figure A6. Contour plot for contact forces between for nozzle size 300 µm and the needle

length 0.25 mm.

4) At nozzle size 300 μm and the needle length 0.5 mm
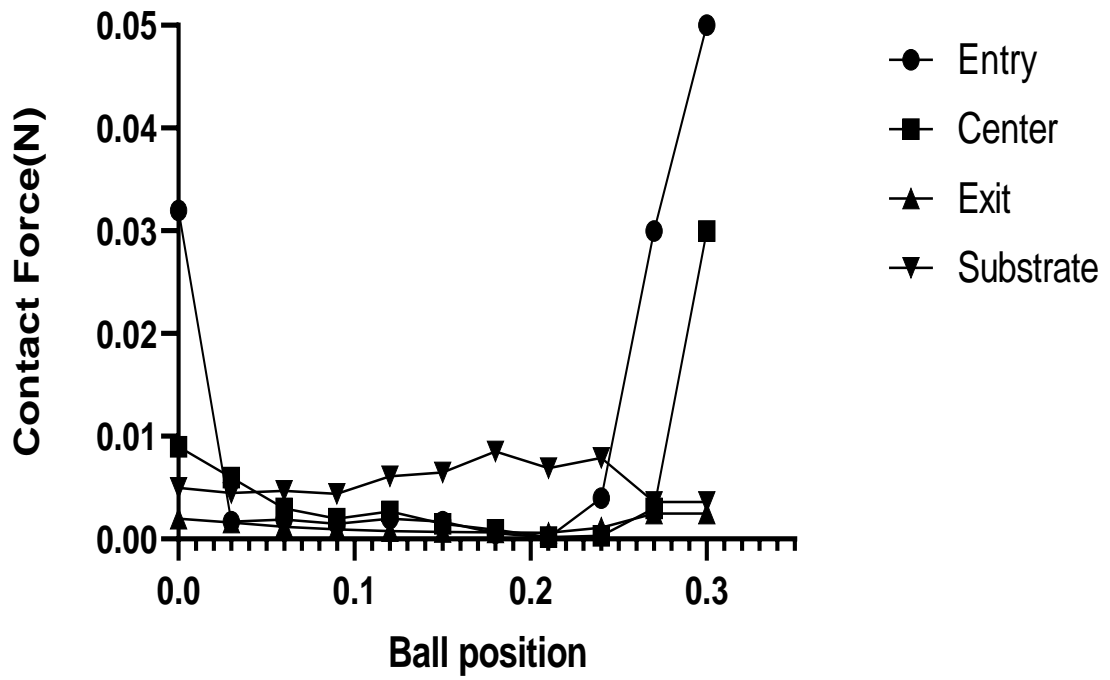
Figure A7. Contact forces vs ball position graph at various locations of the model for nozzle size 300 µm and the needle length 0.5 mm.
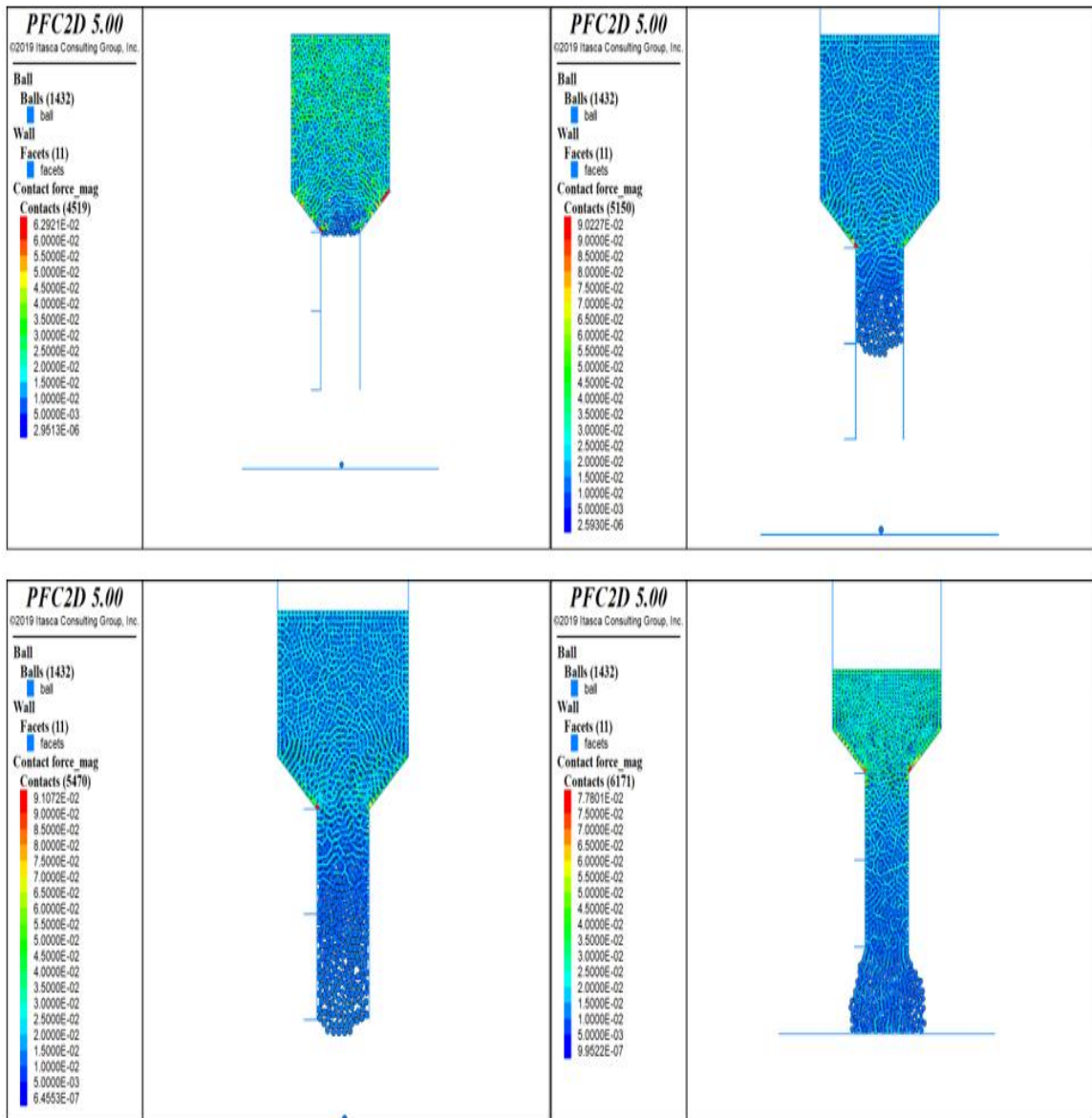
*Figure A8*. Contour plot for contact forces between for nozzle size 300 µm and the needle

length 0.5 mm**.**

5) At nozzle size 300 µm and the needle length 1 mm
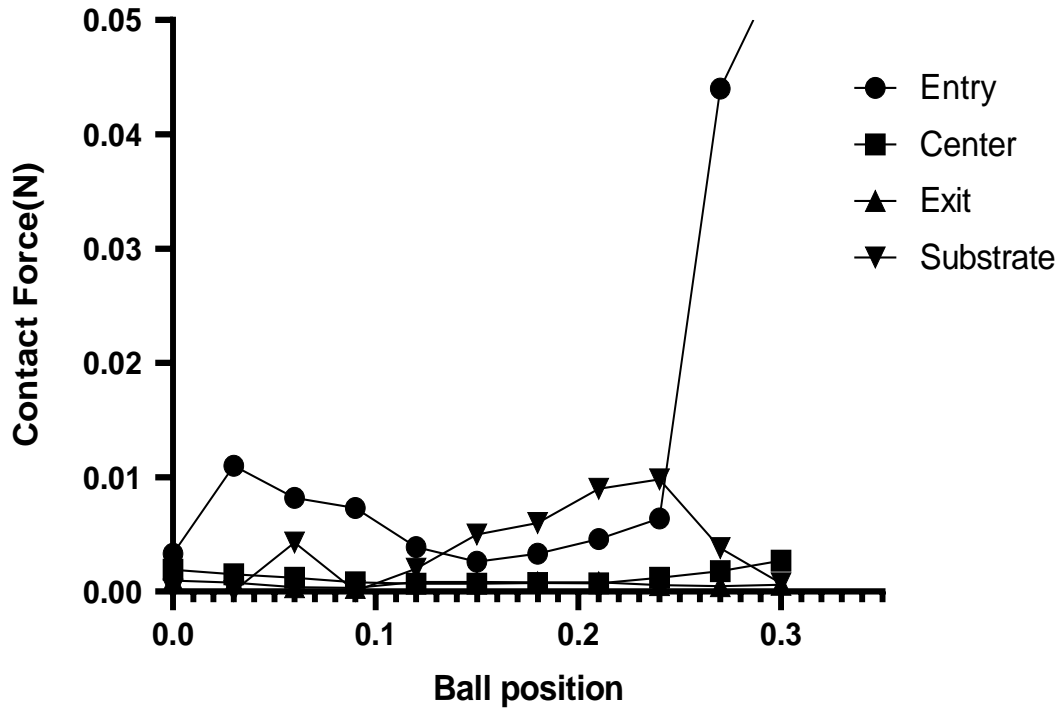
*Figure A9*. Contact forces vs ball position graph at various locations of the model for nozzle

size 300 µm and the needle length 1 mm.
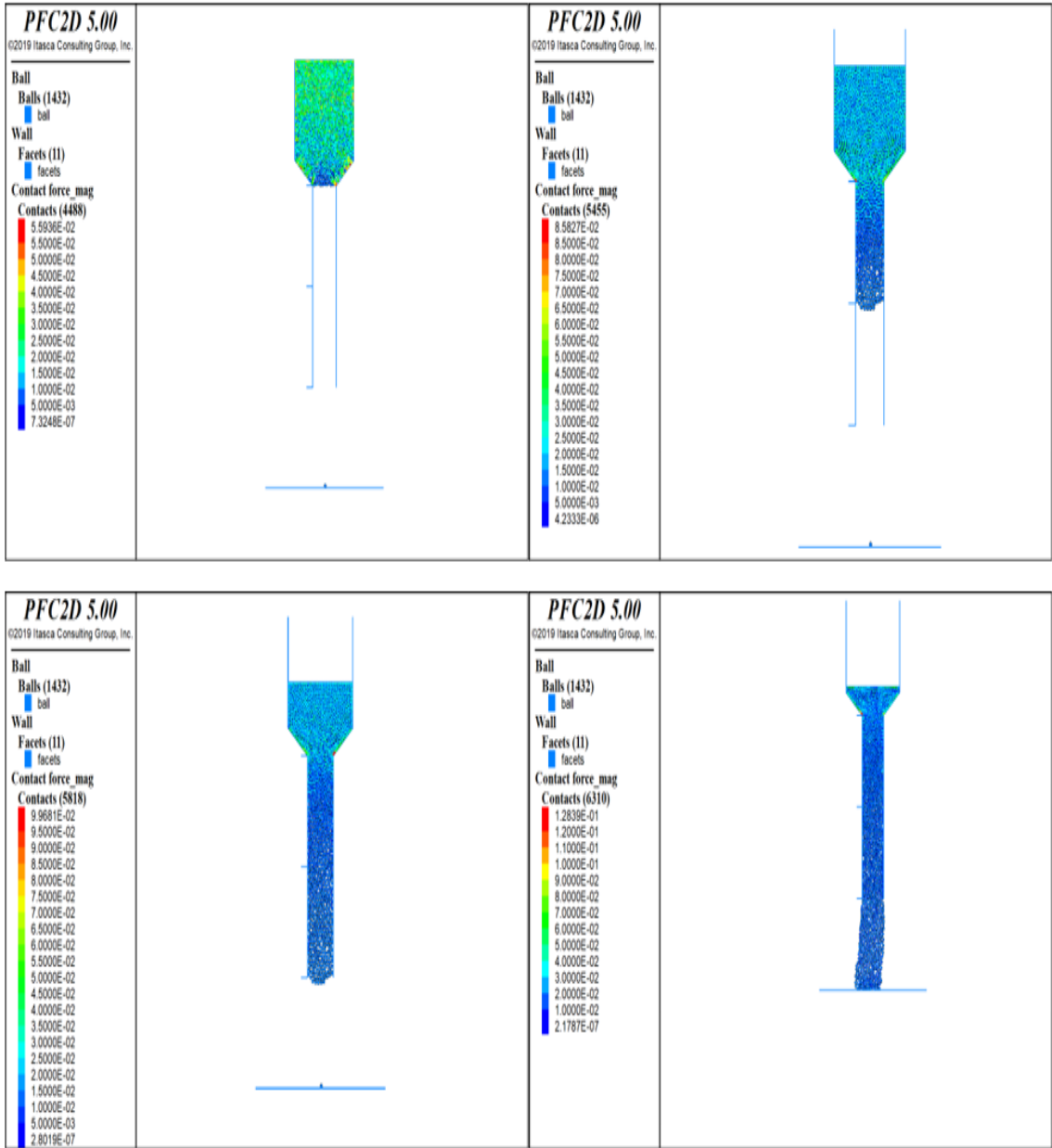
Figure A10. Contour plot for contact forces between for nozzle size 300 µm and the needle

length 1 mm.

6) At nozzle size 400 µm and the needle length 0.25 mm
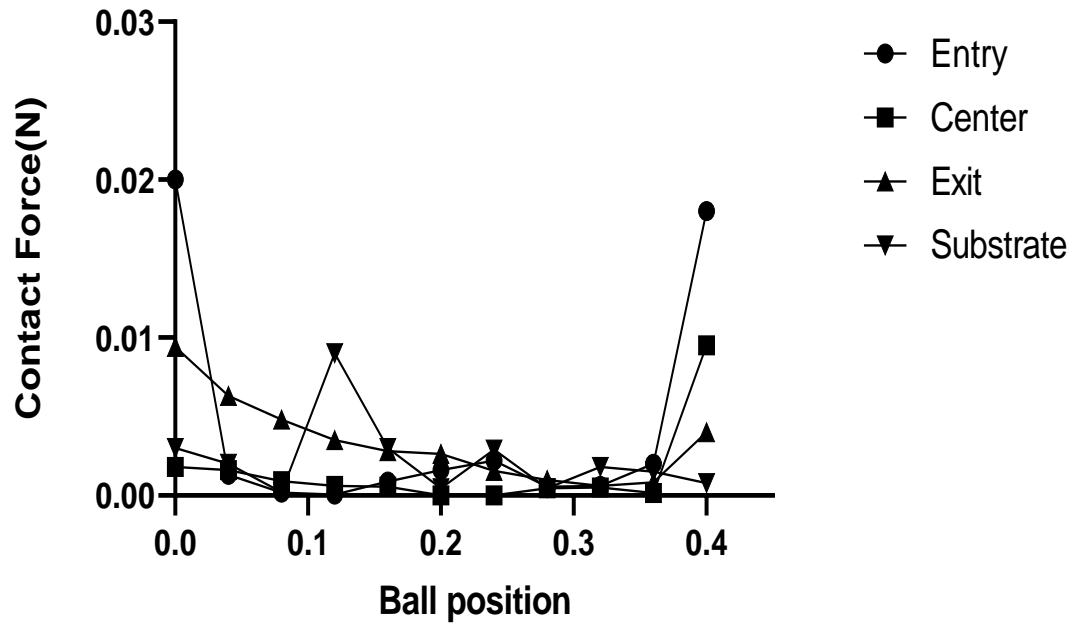
Figure A11. Contact forces vs ball position graph at various locations of the model for nozzle size 400 µm and the needle length 0.25 mm.
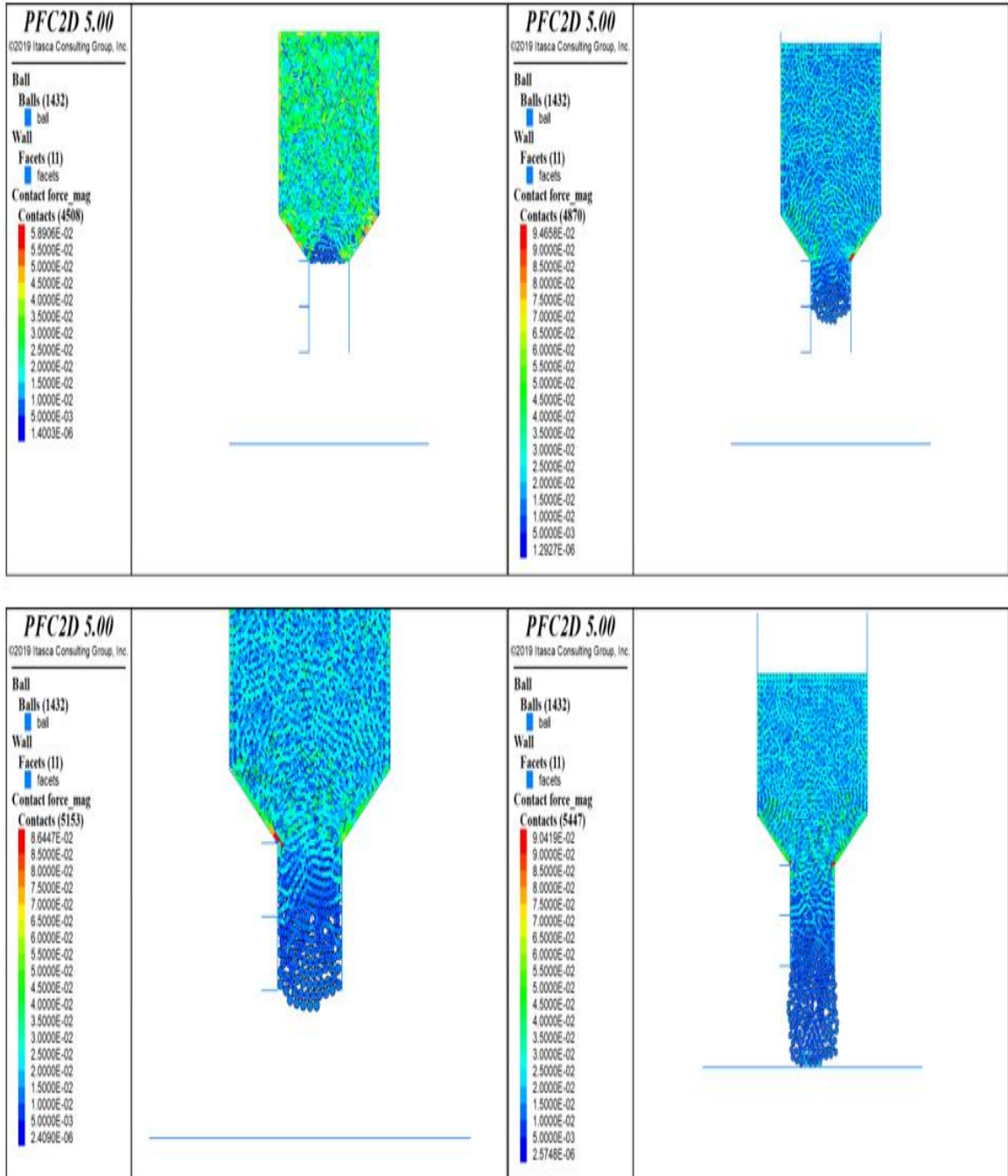
Figure A12. Contour plot for contact forces between for nozzle size 400 µm and the needle

length 0.25 mm.

7) At nozzle size 400 µm and the needle length 0.5 mm
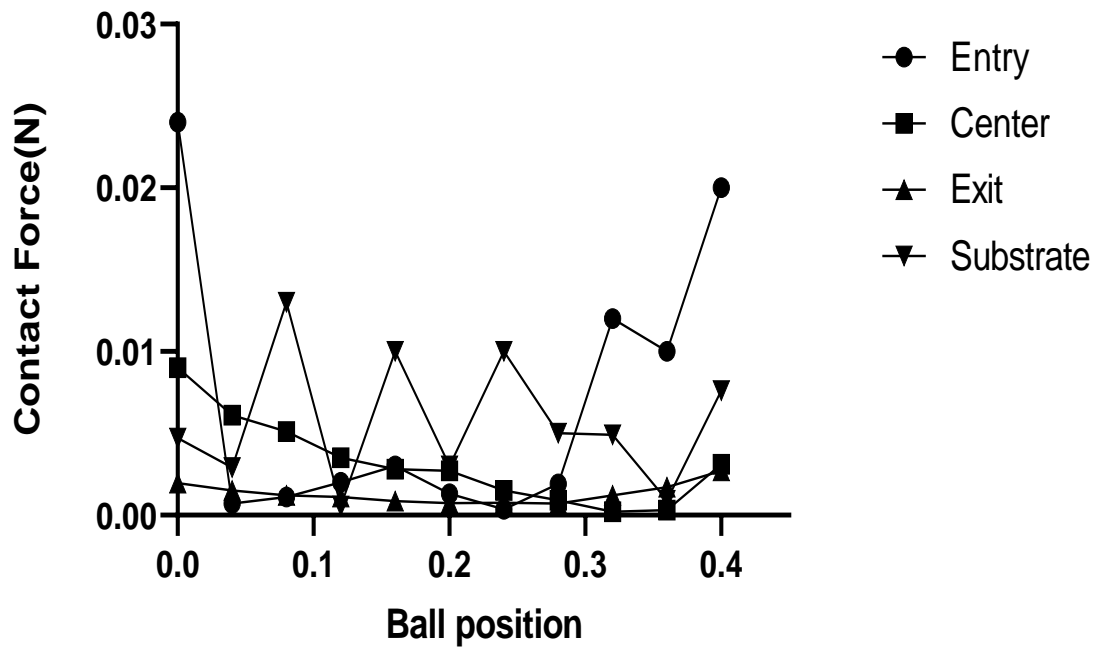
*Figure A13*. Contact forces vs ball position graph at various locations of the model for nozzle size 400 µm and the needle length 0.5 mm.
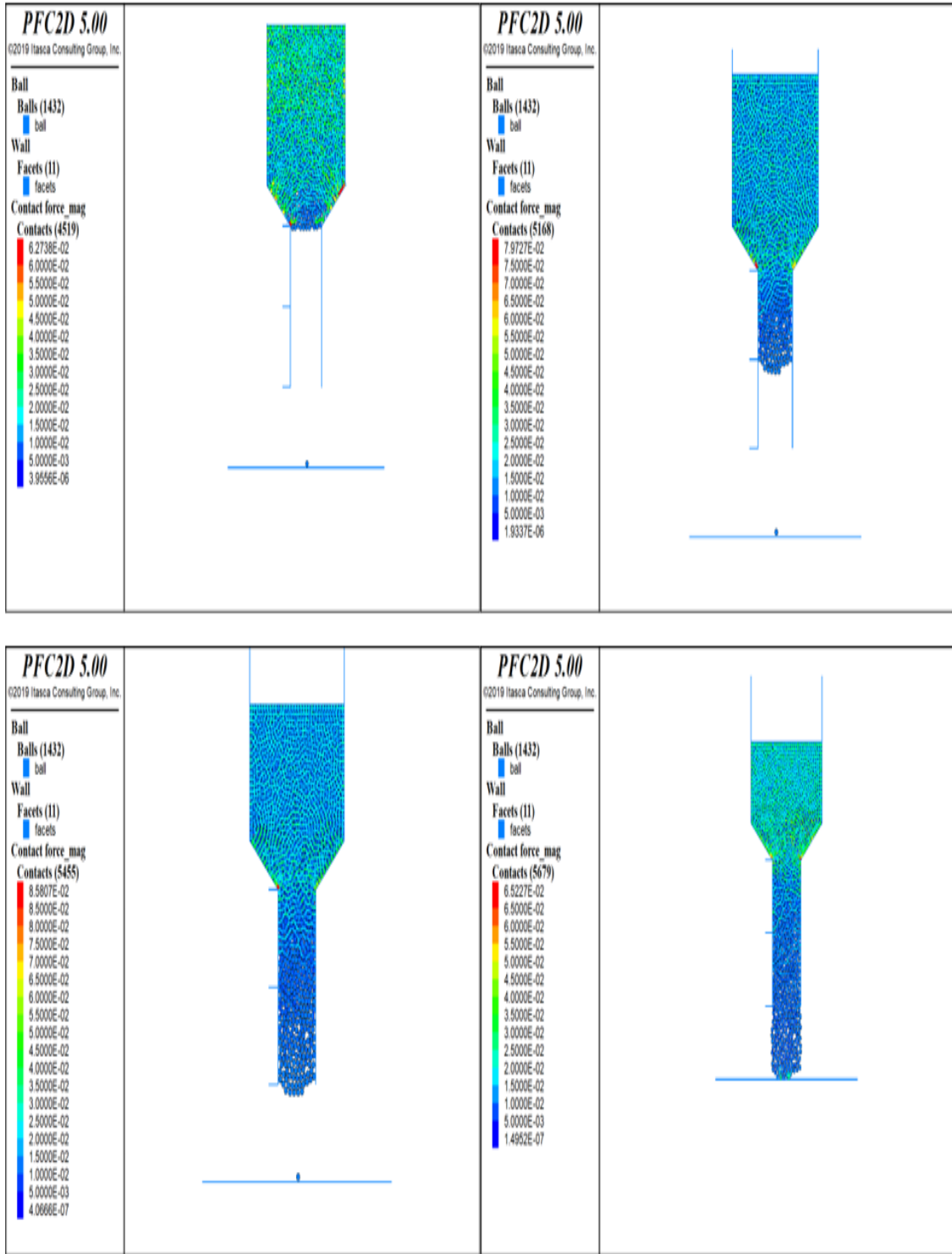
*Figure A14*. Contour plot for contact forces between for nozzle size 400 µm and the needle

length 0.5 mm.

8) At nozzle size 400 μm and the needle length 1 mm
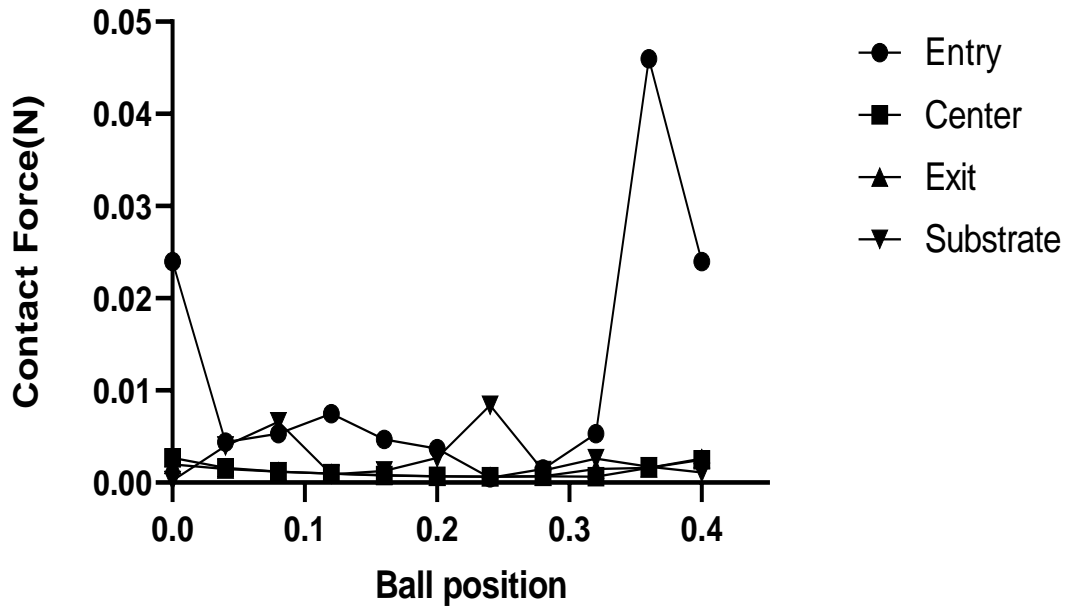
Figure A15. Contact forces vs ball position graph at various locations of the model for nozzle size 400 µm and the needle length 1 mm.
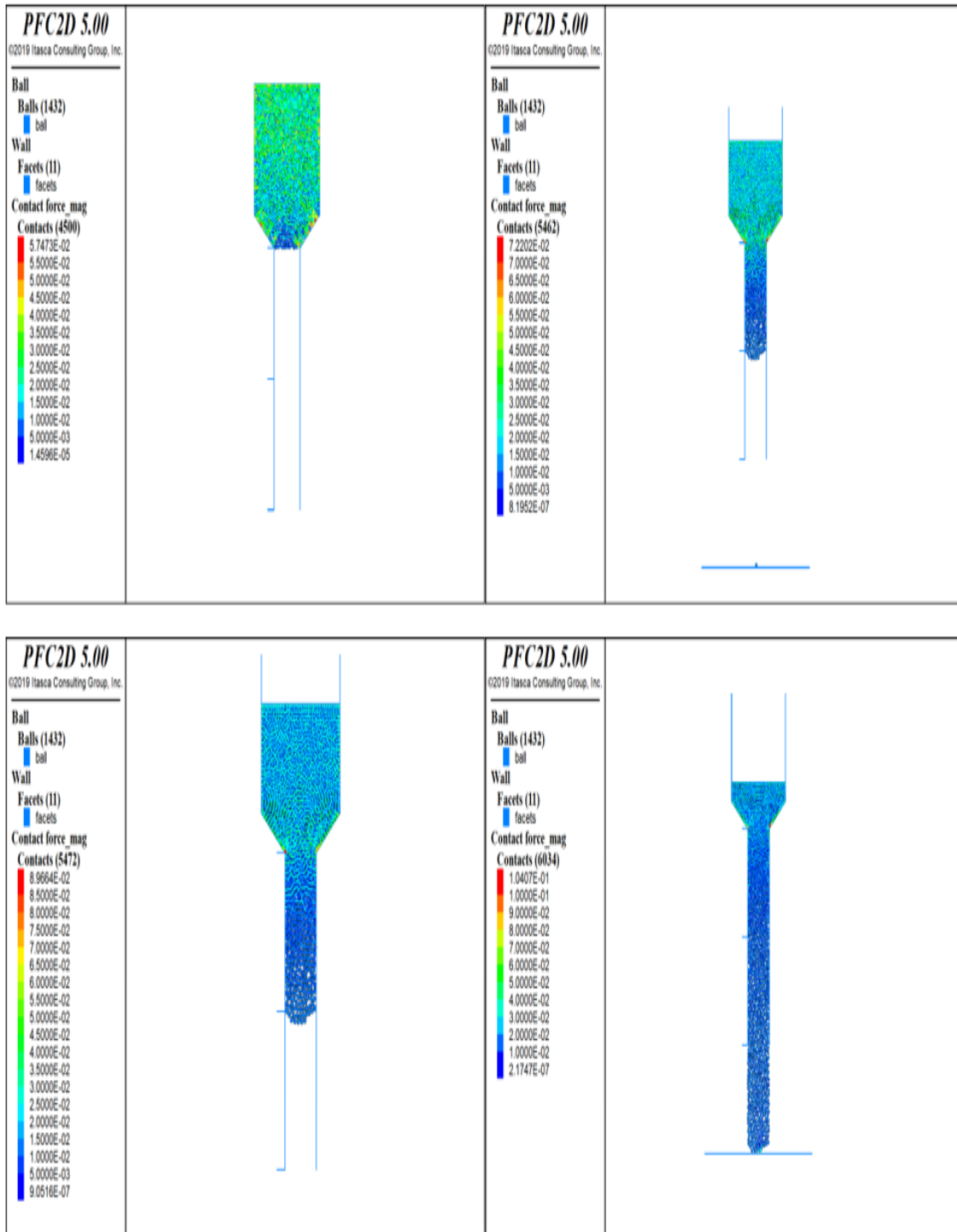
Figure A16. Contour plot for contact forces between for nozzle size 400 µm and the needle length 1 mm.

9) At nozzle size 500 µm and the needle length 0.25 mm
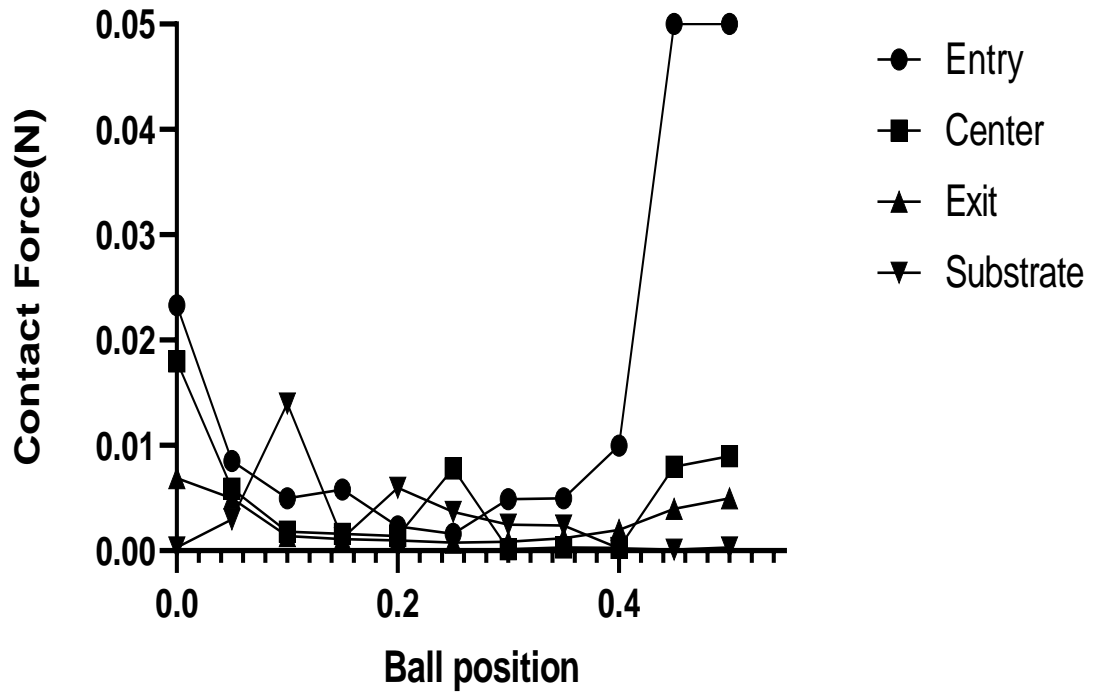
Figure A17. Contact forces vs ball position graph at various locations of the model for nozzle size 500 µm and the needle length 0.25 mm.
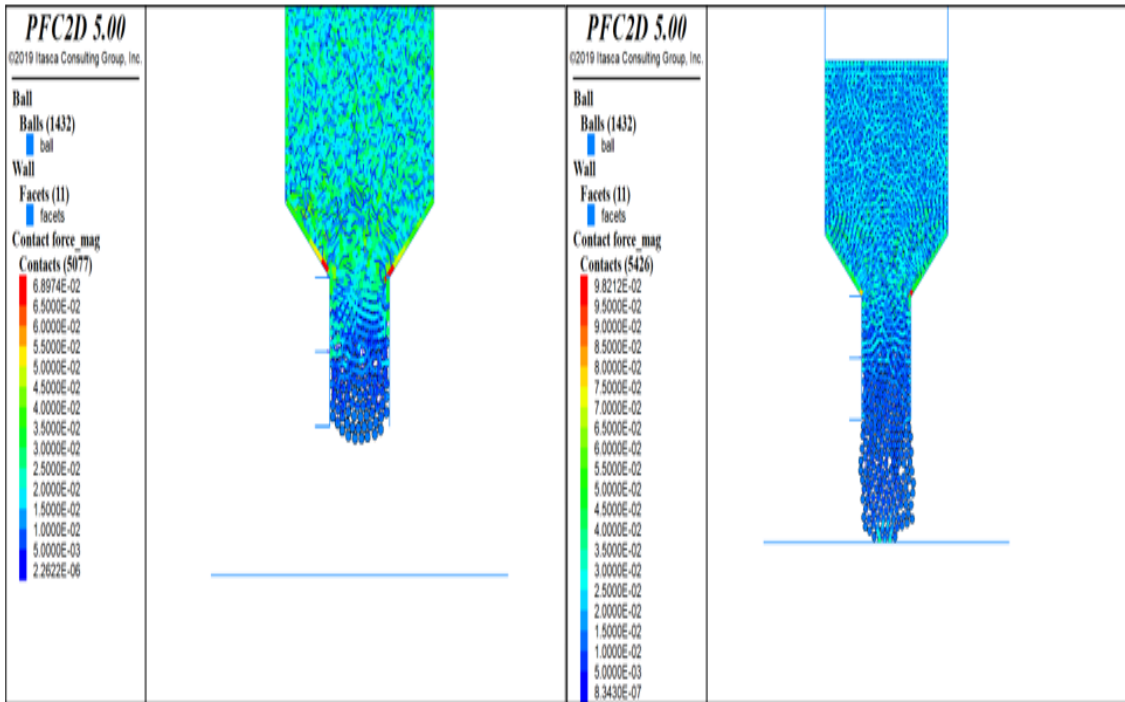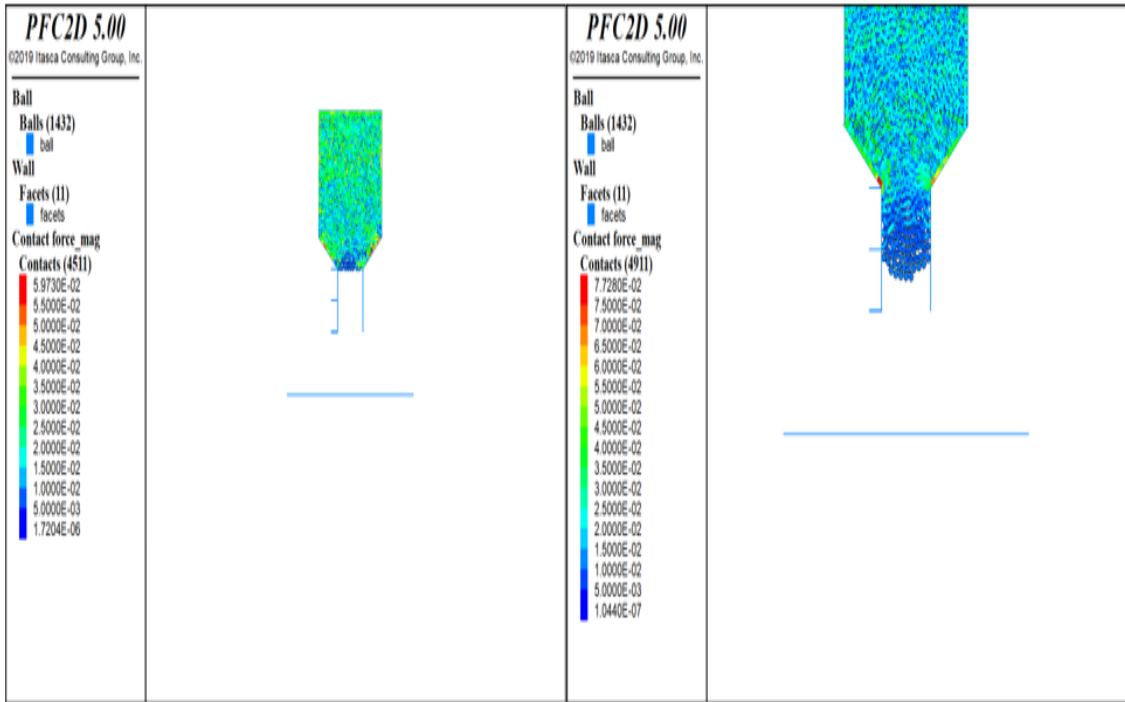
Figure A18. Contour plot for contact forces between for nozzle size 400 µm and the needle

length 0.25 mm.

10) At nozzle size 500 µm and the needle length 0.5 mm
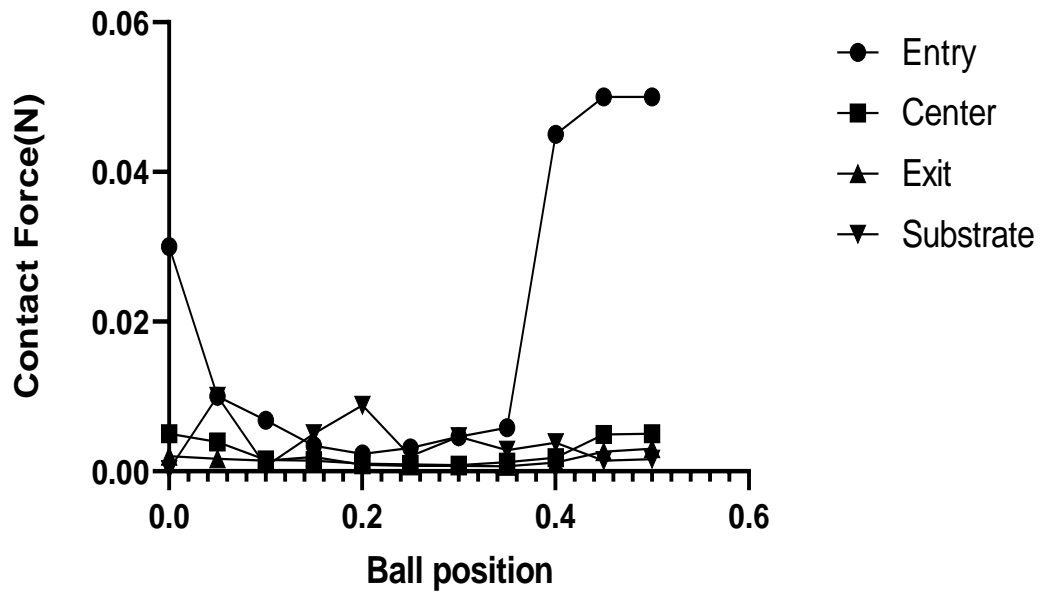
Figure A19. Contact forces vs ball position graph at various locations of the model for nozzle size 500 µm and the needle length 0.5 mm.
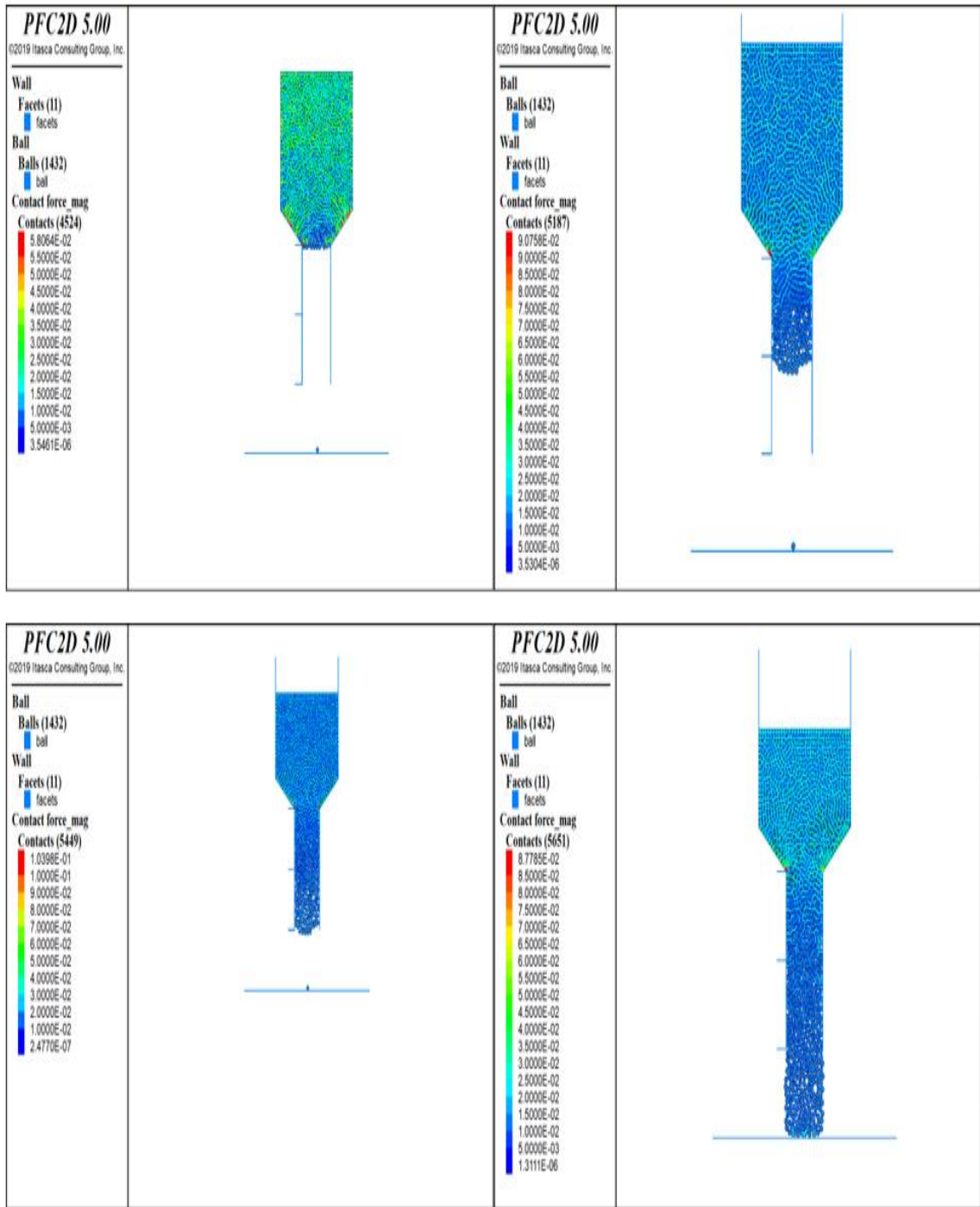
Figure A20. Contour plot for contact forces between for nozzle size 500 µm and the needle

length 0.5mm.

11) At nozzle size 500 μm and the needle length 1 mm
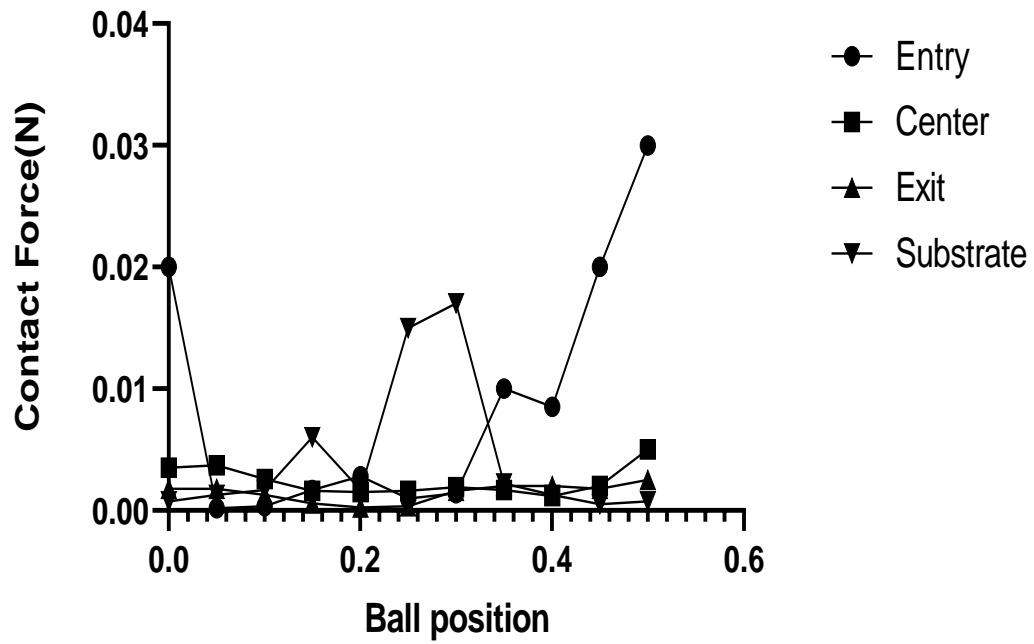
*Figure A21*. Contact forces vs ball position graph at various locations of the model for nozzle size 500 µm and the needle length 1.0 mm.
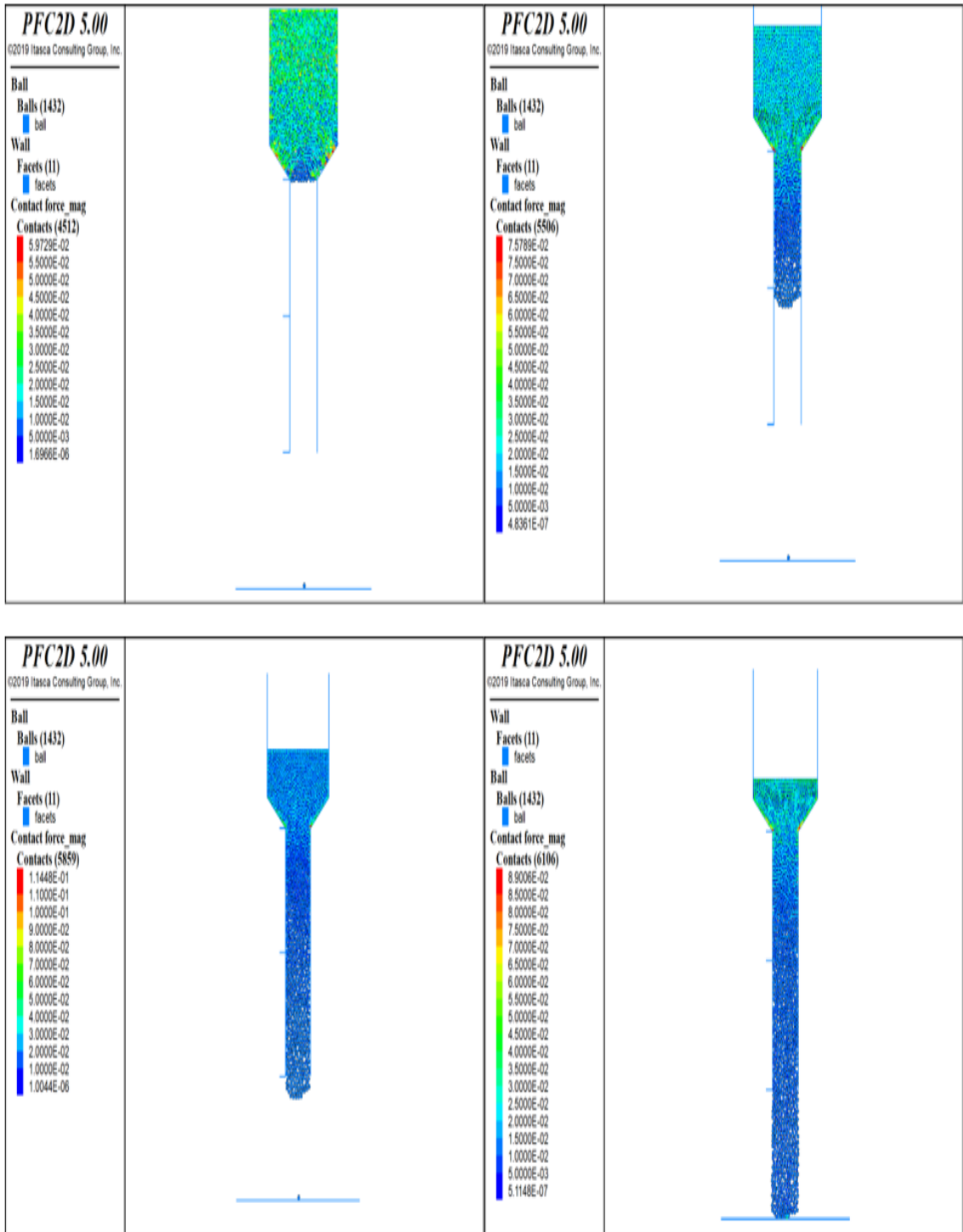
Figure A22. Contour plot for contact forces between for nozzle size 500 μm and the needle

length 1.0 mm